Feasibility of Passive Acoustic Detection of Coronary Artery Disease Utilizing Source Separation

Daniel Boyd Cooper

Thesis submitted to the faculty of the Virginia Polytechnic Institute and State University
in partial fulfillment of the requirements for the degree of

Master of Science
In
Biomedical Engineering

Pavlos P. Vlachos, Committee Chair
Michael J. Roan, Member
Raffaella De Vita, Member

December 1st, 2010
Blacksburg, Virginia USA

Keywords: Coronary Artery Disease, Phonoangiography, Acoustic Source Separation

Feasibility of Passive Acoustic Detection of Coronary Artery Disease Utilizing Source Separation

Daniel Boyd Cooper

ABSTRACT

Coronary artery disease (CAD) remains the leading cause of death in both the United States and the world at large. This is primarily due to the extreme difficulty associated with preemptive diagnosis of CAD. Currently, only about 20% of all patients are diagnosed with CAD prior to the occurrence of a heart attack. This is the result of limitations in current techniques, which are either noninvasive, extremely expensive, or have very poor correlation with the actual disease state of the patient. Phonoangiography is an alternative approach to the diagnosis of CAD that relies upon detection of the sound generated by turbulent flow downstream from occlusions. Although the technique is commonly used for the carotid arteries, in the case of the coronary arteries the technique is hampered by signal-to-noise problems as well as uncertainty regarding the spectral characteristics associated with CAD. To date, these signal processing difficulties have prevented the use of the technique clinically. This research introduces an alternative approach to the processing of phonoangiographic data based upon knowledge of the acoustic transfer within the chest. The validity of the proposed approach was examined using transfer functions which were calculated for 14 physiologically relevant locations within the chest using a 2-D Finite Element Model (FEM) generated from physiologic data. These transfer functions were then used to demonstrate the technique using test cases generated with the FEM. Finally, the vulnerability of the technique to noise was quantified through calculation of matrix condition numbers for the chest acoustic transfer at each frequency. These results show that while in general the technique is susceptible to noise; noise tolerance is greatly improved within the frequency range most likely to correspond to an occlusion. Taken together, these results suggest that the proposed technique has the potential to make phonoangiography viable as a screening technique for CAD. Such a technique would greatly reduce the cost of CAD, measured in terms of both financial cost as well as lives.

DEDICATION

This work is dedicated to my grandmothers, Virginia Irby Cooper and Mary Ruth Barksdale. The first died of heart disease, while the second has been treated for it. You give me motivation for studying the detection and treatment of coronary artery disease, and add a personal element my graduate work.

ACKNOWLEDGMENTS

Somehow it's fitting that it's three in the morning and I've just finished the final touches on this thesis document, since that seems to be the time of day when the most of the work which went into this thesis was done. For this reason, the first and most appreciative thanks must go to my wonderful wife Michele. You've loved me and understood all the distractions and late nights. You have been with me every step of the way these past two years, and I look forward to all the future years we will have together. I love you with all my heart.

Additionally, I must thank my parents, Gerald and Donna Cooper. Mom, through example you taught me compassion. Somehow I doubt I would have gone chosen biomedical engineering as a profession without that example. Dad, you were my first example of both a man and an engineer, and my first mentor technically. Both of you raised me right and set me on the proper path and I am forever indebted to you both. Thomas, you may not have ever realized it, but there are thanks due to you as well. Normally the younger brother is pushed to live up to the example of the older brother; I was pushed to set a high bar because I knew you were following behind me, and you would be trying to break it. Thanks also go to my fellow members of the "ESM Trio", Matt Dunham and David Freeman. I have the opportunity to be here because I graduated ESM; I'm not sure that would have happened without the two of your to go through it with, so thanks.

Professionally, thanks must go to the members of the AEThER lab. Very rarely is any work done by a single individual in a vacuum, and this is no exception. Satyaprakash Karri, John Charonko, Chris Weiland, and David Griffiths, the four of you in particular have served as examples for me in one way or another during our time in the lab together. David Hubble, Justin Dominic, Kelley Stewart, Jamie Schmieg, and Sam Raben, all of you have contributed to this work and helped this work in some way. I appreciate your help, and look forward to continuing in the lab with you, as well as the rest of the members of the lab.

Dr. Raffaella De Vita, thank you for being willing to serve on my committee on short notice; I truly appreciate it. Dr. Michael Roan, thank you for serving on my committee and for all your insights into both acoustics and signal processing. Primacy among my professional thanks, however, must go to my committee chairman, Dr. Pavlos Vlachos. You were impressed enough with me through my senior design project to take me into your lab and to be committee chair, which I thank you for. You have been a professional example for me, and I look forward to continue studying under you as I pursue my Ph.D.

Finally, thanks must go to God Almighty. Everyone else listed here was important in helping me with the work on my thesis, or played a role in making me who I am today. Without You, however, I would not be, nor would I be freed from my sins. Therefore, the ultimate thanks are Yours and Yours alone. We may study physics, but it is You who made physics. We study, derive and analyze equations, but it is You who put them into effect and breathes life into them:

πάντα δι' αὐτοῦ ἐγένετο καὶ χωρὶς αὐτοῦ ἐγένετο οὐδὲ ἕν ὃ γέγονεν

All things came into being through Him, and apart from Him nothing came into being that has come into being. – John 1:3

TABLE OF CONTENTS

LIST OF FIGURES

LIST OF TABLES

LIST OF SYMBOLS

Frequency ..... f
Angular Frequency ..... ω
Source strength vector ..... $\mathbf{s}$
Surface velocity vector ..... $\mathbf{v}$
Mixing matrix..... $\mathbf{H}$
Demixing matrix..... $\mathbf{W}$
Singular value matrix..... $\mathbf{\Sigma}$
Acoustic pressure ..... P
Matrix condition number..... k
Observed Order of accuracy (mesh convergence)..... p
Mesh Refinement Factor..... r
Approximate source strength vector..... $\hat{\mathbf{s}}$
Approximate surface velocity vector..... $\hat{\mathbf{v}}$
Relative error in the source strength vector..... δs
Relative error in the surface velocity vector..... δv
Error amplification factor..... β

LIST OF EQUATIONS

$$k(\mathbf{A}) = \frac{\max(\Sigma)}{\min(\Sigma)}$$

$$\delta s \le k(\delta H + \delta v)$$

$$\delta s = \frac{\|\mathbf{s} - \hat{\mathbf{s}}\|}{\|\mathbf{s}\|}$$

$$\delta s = \beta \delta v$$

$$FLOW = \pi R^2 \rho \frac{d^2 u}{dt^2}$$

$$FLOW = j\omega \pi R^2 \rho \frac{du}{dt}$$

1. Introduction & Prior Art

1.1. Coronary Artery Disease

Coronary artery disease (CAD) is currently the leading cause of death in both the United States and the world[1]. In 2009, CAD was responsible for more than 20% of all deaths within the United States and had a total financial cost of $165.4 billion USD[2]. CAD occurs due to the buildup of atherosclerotic plaques in the coronary arteries, which are responsible for providing oxygenated blood to the heart muscle itself. While these plaques themselves are often asymptomatic, these plaques can rupture, exposing the thrombogenic core of the plaque to the blood and triggering clot formation[3]. These clots can then flow downstream and block arteries, resulting in a myocardial infarction, commonly known as a heart attack. Significantly, this means that CAD can progress suddenly, and without warning, to an infarction.

However, the process of plaque rupture provides only a partial explanation of the extremely low rate of CAD diagnosis that was discussed previously. Much of the reason for this is due to the limitations of current technology for CAD diagnosis. To be useful for CAD screening, a technique needs to be relatively inexpensive and noninvasive, but also relatively accurate. No currently available technique is able to meet these criteria, as shown in Figure 1-1, which categorizes available techniques[4, 5]. The current gold standard for CAD diagnosis remains x-ray angiography, which images arteries using a contrast agent which allows arteries to appear on x-ray images. X-ray angiography is relatively inexpensive and quite accurate, but requires coronary catheterization, which requires hospitalization and exposes the patient to significant risk. Intravascular ultrasound (IVUS) detects CAD using an ultrasonic probe attached to a catheter, which allows imaging of arterial walls. Although the technique is accurate, like x-ray angiography it requires catheterization. Due to the risks associated with catheterization, these techniques are not used unless the presence of CAD is already suspected.

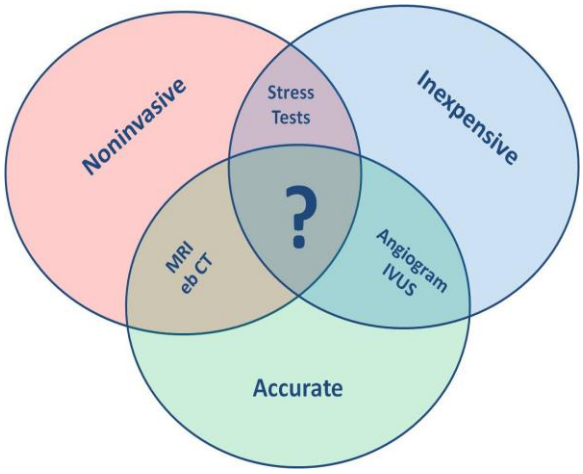

Figure 1-1: Schematic representation of the current state of the art for CAD diagnosis. Techniques fall into three different categories, categorized by the limitations of the techniques, which are either invasive, prohibitively expensive, or insufficiently accurate

Other techniques include magnetic resonance angiography, which uses a contrast agent to make arteries visible on MRI scans, and electron beam CT, which allows rapid imaging of the heart and arteries. These techniques are relatively accurate, but require large, specialized, and expensive equipment. As a result, like invasive techniques, these techniques are useful only when CAD is already suspected, but the techniques cannot be practically implemented for general screening of the population. Stress tests involve challenging the patient with exercise, and monitoring the heart for signs of ischemia using EKG, and are currently the only diagnostic modality used for CAD screening. Unfortunately, studies have shown that stress test results have very poor correlation with actual heart attacks[6]. This is most likely due to the previously discussed role of plaque rupture; plaques that are sufficiently

small to have little impact on blood flow are still vulnerable to sudden rupture and produce clots.

1.2. CONCEPT OF PHONOANGIOGRAPHY

Phonoangiography is a diagnostic technique that seeks to detect CAD noninvasively through passive detection of the sounds associated with CAD. The underlying concept is quite simple. Under normal circumstances, blood flow through the circulatory system is laminar in nature [Insert citation]. However, in the case of CAD, obstructions in the artery can result in transition to turbulence flow[7]. This is significant acoustically because turbulent flow generates broadband sound, while laminar flow is relatively quiet, and what sound is produced is at low frequency. As a result, a diseased artery sounds significantly different from a healthy one. In phonoangiography, the goal is to detect the sounds associated with a diseased artery using a microphone or an array of microphones located on the chest surface. This type of approach is already applied to the detection of carotid artery disease, where the sounds associated with a blocked artery are known as "*bruits*" (the French word for sound). Because the carotid arteries are so close to the surface of the neck, carotid blockages are commonly detected simply by listening to the artery using a common stethoscope. Thus, the current techniques for the detection of carotid artery disease represent a validation of the underlying concepts of phonoangiography.

However, for the coronary arteries, clinical and experimental experiences have found the technique to be impractical[8-10]. This is primarily due to two major difficulties associated with actually detecting the sound generated by an occluded coronary artery. First, the sound generated by a diseased artery is relatively faint. In the case of the carotid arteries, this is mitigated against by their superficial position. In contrast, the coronary arteries are located relatively deep within the chest behind a layer of bone (the sternum and rib cage). As a result, the acoustic signature reaching the skin surface in CAD is significantly less than the sound reaching the surface in carotid artery disease. The other main difficulty is due to the other sources of sound generation located within the chest. The circulatory, respiratory, and even digestive systems all produce large amounts of noise, even under normal, healthy conditions. As a result, the sounds generated by a diseased coronary artery are often drowned out by a din of background noise.

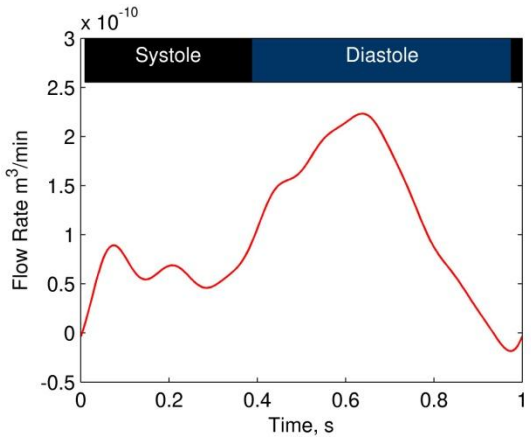

Figure 1-2: Flow waveform for the coronary artery. Flow in the coronary peaks during diastole, when the heart muscle relaxes. This is in contrast to the result of the circulatory system, where peak flow occurs when the heart contracts at systole[3].

Fortunately, this affect is reduced by the nature of coronary blood flow. As shown in Figure 1-2, peak flow (and peak sound generation) occurs during diastole, when the heart is relaxed. In contrast, the rest of the circulatory system experiences peak flow and generates the most sound during systole, when the heart contracts. Thus, the severity of the background noise is reduced when signal strength is strongest. Despite this beneficial effect, background noise remains a major difficulty in efforts to perform phonoangiography.

The net effect of these two factors (faint signal and high background noise) is that phonoangiography can be cast as the detection of a faint signal in a noisy environment. As a result, sophisticated signal processing techniques are required to perform CAD; a schematic representation of the current paradigm is shown

in Figure 1-3. Previous attempts have used techniques as varied as spectral feature detection, phased array techniques, and fractal analysis of acoustic signals. Unfortunately, as discussed in the following section, the sounds generated by stenosed arteries are irregular and differ between blockages. This makes an already difficult signal processing problem even more difficult due to the uncertainty in the characteristics of the signal whose detection is being attempted. A review of experimental and theoretical results examining the fluid flow in stenosed arteries and the sounds produced by such flows is presented next, followed by a discussion of previously developed signal processing techniques which have been applied to phonoangiography. However, to date, no signal processing technique has performed sufficiently to allow for clinical phonoangiography.

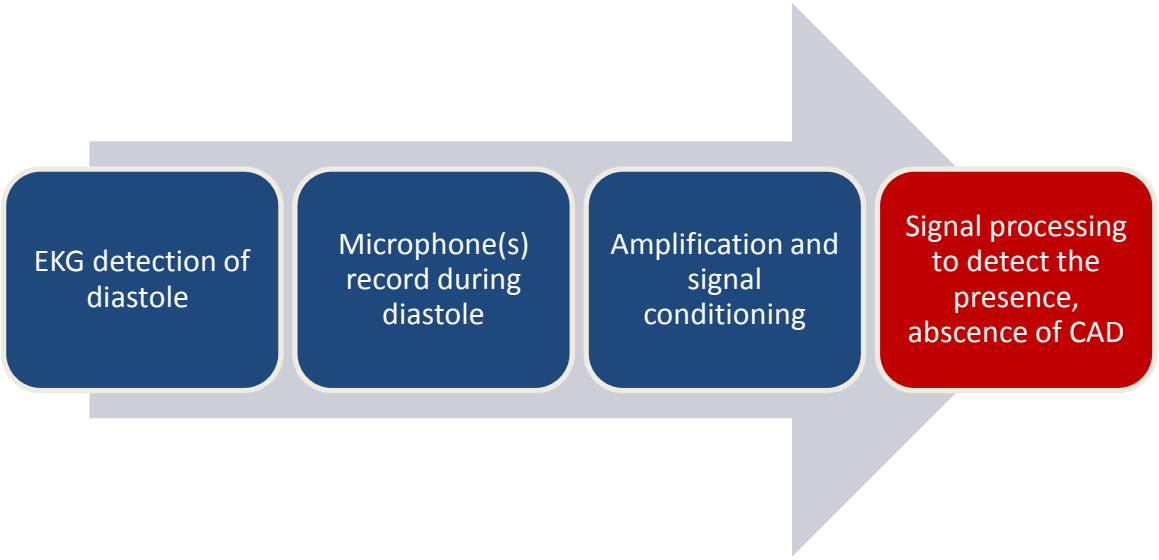

Figure 1-3: Schematic representation of the current paradigm for phonoangiography. Surface acoustic measurements are obtained at the chest surface, which are amplified. Sophisticated signal processing is then applied to detect the presence or absence of CAD. The majority of prior work has focused on the signal processing portion of the system[7].

1.3. Fluid Mechanics of Stenosed Arteries

Under normal circumstances with clean, healthy arteries the coronary artery flows are periodic in time and laminar in nature[11, 12]. Reynolds numbers are on the order of 100, with transition to turbulence in a cylindrical tube occurring at a Reynolds number of 2300[13]. However, in the case of a partially occluded artery, the blockage acts in similar manner to a nozzle, and turbulence can occur. This turbulence results from the development of a strong shear layer between the central jet exiting the stenosis, and the recirculation regions located near the wall which develop as a result of flow separation downstream of the stenosis, and has been extensively studied experimentally in both steady and pulastile flow[14-19]. Giddens and colleagues performed a series of experiments studying pulsatile flow through an axisymmetric model of a stenosed artery using laser Doppler velocimetry[20-24]. In these experiments flow separation immediately downstream from the blockage has been shown to occur at Reynolds numbers as low as 10 for a 70% reduction in area stenosis (reduction in lumen area is the measure of stenosis severity most commonly used clinically)[25]. Moreover, such a stenosis was found to lead to turbulence at Reynolds numbers as low as 300. In a pulsatile flow, this generation of turbulence becomes time dependent, reaching its peak during flow deceleration, and being minimized during flow acceleration[25]. However, for stenoses of 50% of greater reduction of area, turbulence has been shown to

be generated throughout the flow cycle[22]. It is important to note that while this flow separation leads to the development of turbulence in the flow, this turbulence is at its strongest 6-12 diameters downstream from the blockage[26, 27].

More recently, numerical simulations have allowed more detailed examinations of turbulent flow downstream from stenoses. Stroud et al. performed computational fluid dynamics (CFD) simulations of flow through a model of the carotid artery based upon a specimen obtained from an endarterectomy. This model was tested with steady flow at Reynolds numbers of 300, 600, and 900, using both the Chien and Goldberg varieties of the k-ε turbulence model. The velocity profiles calculated in this study was compared to experimental data from Giddens and colleagues, and good agreement was obtained[20]. These results showed the presence of vortex separation downstream from the blockage, but suggested that the flow was actually transitional, rather than fully developed turbulence, based upon the ratio of turbulent and laminar viscosity[28]. Mittal et al. simulated pulsatile flow through a planar channel with a semicircular blockage using direct numerical simulation (DNS) as well as large-eddy simulation (LES), the validity of which for stenotic flow has been studied by Varghese et al., who compared LES with results with DNS and found agreement[29]. These simulations revealed in greater detail the previously described role of the shear layers separating the central jet from the recirculation near the wall in driving the turbulent flow. Moreover, these studies suggested that the flow first transitions to turbulence downstream of where the flow reattaches to the channel walls[30].

In a more recent series of simulations, Varghese et al. performed DNS simulations of stenotic flows with a 75% reduction in area under both steady and pulsatile flow conditions at Reynolds numbers of 500 and 1000. The steady flow simulations flowed transition to turbulence about five diameters downstream from the stenosis through the breakup of streamwise hairpin vortices. This mechanism for transition to turbulence is in agreement with that predicted by the DNS simulations of Sherwin and Blackburn, who moreover were able to characterize the transition as a subcritical period double bifurcation[31]. In addition, the simulations also considered the effect of eccentricity in the stenosis, and found that an eccentricity of 5% of the vessel diameter was sufficient to cause the jet to deflect towards the wall, causing it to break down at sufficiently high Reynolds numbers[32]. In the case of the pulsatile flow, introduction of stenosis eccentricity also resulted in localized, periodic transition to turbulence. The pulsatile simulations also supported the experimental results that suggested that peak turbulence occurred during flow deceleration, which they suggested was due to breakdown of streamwise vortices formed during the acceleration of the flow[33, 34]. These simulations predicted a turbulent velocity spectra with a broadband nature with a -5/3 slope that is common in turbulent flows[32]. The simulations by Mittal et al. suggest that the behavior is more complicated than this, with the proper choice of slope depending on the frequency range of interest, but they also report broadband velocity spectra behaves in a similar manner to that reported by Varghese over a substantial portion of the frequency range[30]. A recent series of experiments by Karri & Vlachos, which utilized digital particle image velocimetry (DPIV) to study pulsatile flow through asymmetric stenotic arteries; these experiments also show broadband velocity spectra, validating the experimental conclusions discussed previously[35].

1.4. Sound Generation by Stenosed Arteries

Because the velocity spectra downstream from the stenosed region of the artery is broadband in nature, one might expect a stenosed artery to produce broadband noise over a large frequency range. However, both experimental and analytical literature suggests that the situation is somewhat more complicated. The vast majority of these studies have suggested that the acoustic pressure spectra generated by a stenosed artery consists of two narrowband peaks. Akay et al. recorded the sounds produced downstream of an occlusion (with a 72% reduction in area) artificially generated in the femoral arteries of dogs, and analyzed the sounds using both discrete Fourier transforms (DFT) and autoregressive (AR) methods. The

averaged spectra (over 75 periods) showed a narrowband peak at a frequency of about 400 Hz, as well as a second peak at less than 100 Hz, which was also present in the healthy artery[36]. Similar results were obtained from human patients by Semmlow et al., except that the frequency of the peak associated with coronary artery disease was found to be located between 100-200 Hz, depending upon the level of stenosis[7, 37]. Experiments by Borisyuk which considered steady flow in an elastic tube with a rigid, axisymmetric constriction show similar peaks, except in this data an additional 3rd peak is present in sounds recorded downstream from the obstruction. The frequency range of these peaks agrees well with the results of Semmlow et al[38]. An additional series of experiments by Akay et al. found the peak associated with coronary artery disease to be above 600 Hz.[39, 40]

The patent application of Mohler includes short-time Fourier transforms of the sounds recorded from a patient with known CAD. In this data, narrowband diastolic murmurs with a frequency of approximately 800 Hz were found to be indicative of disease[41]. In a series of benchtop experiments on an experimental model of a stenosed artery, Yazicioglu et al. recorded the pressure spectra generated downstream from a blockage using miniature hydrophones, coupled with measurements of the vibration of the tube wall using laser Doppler vibrometry. These measurements were performed for both rigid tubes, as well as compliant tubes in water and air, at diameter Reynolds numbers of 1000 and 2000. These experiments considered only steady flow. The pressure measurements show broadband noise immediately downstream from the blockage, with narrowband peaks between 100 and 200 Hz occurring further downstream at both Reynolds numbers[42]. These results are similar to those of Borisyuk and Semmlow et al. It is important to note that these results show substantially different behavior in rigid tubes, with a single strong band located at higher frequencies. This suggests that the structural behavior of the tube itself plays a significant role. Additionally, examination of the vibration spectra of the outside of the tube (measured using laser Doppler vibrometry) show the presence of narrowband peaks that occur further downstream, the broadband noise located near the exit of the stenosis is largely absent when the tube is placed in water (this was not observed when the tube was placed in air)[42].

Wang et al. examined the transfer functions associated with a segment of coronary artery. The transfer functions were then used to calculate the sounds output from the artery in response to internal forcing. The authors used the model of Tobin and Chang to determine the internal forcing. This model was fit to experimental data, and predicts broadband noise[27]. The predicted output of the artery, calculated by multiplying the transfer function and the forcing, showed two peaks in the output sounds, similar to those predicted by Semmlow et al. Based upon these results, the authors suggest that the narrowband signals characteristic of stenosed arteries are the result of the broadband turbulent noise exciting the resonant

Author	Approximate Peak Frequency	Flow Condition
Akay et al.	300 Hz	Physiologic
Akay et al.	400 Hz	Physiologic
Semmlow et al.	120 Hz	Physiologic
Borisyuk (1st peak)	110 Hz	Benchtop
Borisyuk (2nd peak)	160 Hz	Benchtop
Akay et al.	600 Hz	Physiologic
Yazicioglu et al.	200 Hz	Benchtop
Mohler	800 Hz	Physiologic

Table 1-1: Summary of the frequencies of reported features associated with CAD. These frequencies are spread throughout a frequency range of 0-800 Hz. Most of these data are from studies on human patients or animal models; the data from Yazicioglu was obtained using a benchtop experiment. The data from Mohler was recorded using short-time Fourier transforms.

modes of the stenosed artery, which leads to narrowband signals located at the resonant frequencies of the artery[43]. The model of Goral-Wojcicka also shows the presence of strong narrow frequency bands in the sounds released by the artery[44]. The different peak frequencies which have been calculated in different studies are summarized in Table 1-1.

1.5. Stationary Spectral Feature Detection

As mentioned previously, the universal starting point in the processing of acoustic signals for phonoangiography is the isolation of the diastolic window of the data. As a result, in a simple, first approach to the acoustic detection of CAD, Semmlow and colleagues, who have performed much of the signal processing work in the field, examined the frequency spectra of acoustic signals recorded during diastole, and examining the ensemble averaged spectra for anomalous high frequency noise[37]. However, while this approach occasionally is successful, often the spectra are not so clearly indicative of the disease state, and this approach is insufficient. As a result, the authors defined the ratio of total acoustic energy above 90 Hz as a diagnostic statistic to determine whether or not CAD was present. The patient was diagnosed with CAD if more energy was contained in the higher frequency range than the lower range. In a small sample of 24 patients, the authors reported that this statistic led to sensitivity and specificity of 83%[37]. Follow-up studies by the group substituted the autoregressive (AR) and later the autoregressive moving average methods (ARMA) for the Fourier transform in an attempt to improve noise tolerance[39, 45, 46]. The sensitivity of these approaches is similar to that obtained using Fourier transforms (85% in the ARMA study). It should be noted, however, that the sample sizes in these follow up studies remained small (15 patients in the AR study, 20 patients in the ARMA study). In all the follow-up studies, the authors continued to use ratio of energy above and below a threshold frequency as the diagnostic statistic. The threshold frequency used was different in each study. A separate study by another group showed that the order of the model used in the AR/ARMA methods is very important, and suggested approaches for selecting the appropriate order[47].

Because the approaches used in previous studies continued to suffer from issues with the high level of background noise, a later study used adaptive line enhancement (ALE) was used to filter the data prior to application of spectral techniques (DFT, AR, ARMA, etc.)[48, 49]. ALE works by attempts to create a reference channel with noise which is similar to that in the actual signal. This reference signal is then subtracted from the original signal prior to further processing. Thus, the end affect of ALE is to apply a form of adaptive noise cancellation. In this study, diastolic recordings from 20 patients were filtered using ALE, and then modeled using both AR and ARMA. The results showed that the use of ALE improved the detection ability of both the AR and ARMA approaches[48]. The patient data used in this study was also used to compare the performance of DFT, AR, and ARMA approaches on the same data (previous studies had used different data in each study). As shown in Table 1-2, the AR and ARMA methods performed similarly, while the DFT and eigenvector method had a higher sensitivity, but lower specificity. However, the eigenvector outperformed the DFT in both categories of performance[50].

1.6. Non-Stationary Spectral Feature Detection

The methods described in the previous section implicitly assume that the signal associated with CAD is statistically stationary, an assumption which is clearly invalid, considering that the signals is being generated by the turbulence produced by pulsatile flow through the stenosis. As discussed in section 1.3, this turbulence may be present only during part of the flow cycle, and even when the turbulence persists throughout the strength of the turbulence is strongly dependent on time. This has lead to several studies examining the use of techniques for non-stationary signals for the detection of CAD. Akay et al. applied zero tracking filters to both the pre- and post-angioplasty signals of the same patients, as well as a population of healthy and known diseased patients[49, 51, 52]. In the first case, the approach successfully

represented the pre-angioplasty and post-angioplasty signal from each patient. In the second study, the technique was shown to have a sensitivity of 84% and a specificity of 81%. However, it should be noted that the threshold value of the diagnostic statistic (which was the mean amplitude of the second zero of the filter during the diastolic window) was chosen to produce the highest percentage of correct identifications, rather than on any physical knowledge or expectation of the system[52]. The same author also attempted the use of fuzzy neural networks, based upon wavelet analysis, to detect CAD. The spectral content at frequencies of 200, 400, and 600 Hz was combined with age, weight, sex, smoking, systolic blood pressure, and diastolic blood pressure were combined to create a feature vector for the neural network. A population of 30 patients (evenly split between healthy and diseased) was used to train the model, which was then applied to the remainder of the available patient population. The model was able to achieve a sensitivity of 85% and a specificity of 89%. The use of wavelet analysis for the acoustic detection of CAD has also been examined by Shertukde, who developed a system which allowed lesion size to be determined from the wavelet coefficients[53]. However, the proposed system was not clinically evaluated.

A company, SonoMedica, Inc. has also produced a device which attempts the phonoangiographic detection of CAD. The prototype device of this company records heart sounds and calculates the short-time Fourier transform (STFT)[41]. The device then examines the frequency, strength, and time-characteristics of the signal to produce a "murmur score", which serves to indicate the likelihood of CAD. An array of sensors is placed at nine different locations on the chest, and a score is calculated at each location, with the final score being taken as the weighted average of the scores from each location. In a clinical study with 113 patients, this approach yielded a sensitivity of 87%, but a specificity of only 52% for male patients. Much better results were obtained with female patients, with a sensitivity of 95% and a specificity of 96%.

Detection Method	**Sensitivity**	**Specificity**
Discrete Fourier Transform (DFT)	75%	62.5%
Autoregressive Model (AR)	72%	88%
Autoregressive Moving Average Model (ARMA)	71%	88%
Eigenvector Methods (Minimum norm)	91%	79%
Zero-tracking filters	84%	81%
Neural Networks	85%	89%
STFT-based murmur score	95%	96%

Table 1-2: Sensitivity and specificity values calculated from the spectral analysis of diastolic heart sounds. Note that methods listed in normal text assume stationary signals, while those listed in italics are designed for non-stationary signals. Among the stationary techniques, the DFT method had better sensitivity but less specificity than the AR and ARMA methods, which performed similarly. The eigenvector method had by far the best sensitivity, but its specificity was inferior to that of the AR and ARMA methods. Both zero-tracking filters and neural networks outperformed the stationary techniques, while the best performance was the murmur score based upon STFTs calculated by the SonoMedica, Inc. prototype.

1.7. NON-SPECTRAL DETECTION

A major limitation of the previously described spectral techniques, regardless of whether they are stationary or non-stationary, is the requirement of some *a priori* knowledge about the acoustic signature of diseased coronary arteries, and also the assumption that something about this noise is unique in comparison to all other signals produced *in vivo*. It has been apparent even from the early work of

Semmlow et al. [37, 45] that there is not a uniform signature corresponding to CAD in all patients. As a result, several non-spectral approaches have been attempted. Padmanabhan et al. attempted to detect CAD by attempting to measure the fractal dimension of the diastolic heart sounds[54]. The idea underlying this approach was that the turbulence (a chaotic process) producing the noise in diseased arteries. As a result, a fractional dimension, representing the presence of chaos in the sounds, and hence indicating the presence of CAD. Unfortunately, while the approach was shown to work extremely well on noise-free signals, the sensitivity of the algorithm to noise caused the approach to fail when even moderate amounts of noise are encountered[54].

Another approach was taken by Xiao et al., who looked for differences between resting and exercise phonocardiograms[55]. The primary metric for the detection of CAD in these studies was the ratio of the S1 amplitudes in the resting and exercise phonocardiograms. The authors determined that a ratio greater than three was indicative of a disease state; no reason was given to justify this threshold. However, this approach is extremely dependent upon the individual patient, as the appropriate level of exercise is different for different individuals, and an appropriate level is not clear. This represents a major limitation of the technique. Zhao studied the use of instantaneous frequency to detect CAD, which has been previously shown to be of use in analyzing heart valve sounds[56, 57]. In this work, a learning algorithm was used to analyze the statistical properties of the weighted instantaneous frequency function, which was trained with a set of 40 evenly split patients. The authors reported a sensitivity of 85%, with a 100% specificity[56].

Most relevant to the current work are those studies which have utilized signals from multiple microphones to detect CAD, known as array phonoangiography. Owsley et al. used an array of microphones to create an image of the energy distribution within a model of the body. This was done utilizing nearfield (focused) beamforming [58, 59]. The advantage of such a technique is that it permits spatial separation of the sounds associated with CAD, as well as the spectral and temporal separation which are allowed by the previously described spectral and non-spectral techniques. The technique produced good results for acoustic phantoms, but has not been able to produce reliable results in human subjects[7]. Another similar approach was taken by MedAcoustics, Inc., who took a phased-array approach to the detection of CAD[7]. The array used in this study consisted of rows of contact microphones, so as to provide directional sensitivity. Unfortunately, the technique works well only in the farfield. In the case of CAD, this would require microphones to be placed more than 5 feet away from the chest, which causes such approaches to be ineffective when used with surface microphones.

2. SOURCE SEPARATION PHONOANGIOGRAPHY: THEORY AND METHODS

2.1. INTRODUCTION

In reviewing the previously discussed attempts to detect the sounds associated with a diseased artery, the ultimate conclusion is that conventional techniques are simply incapable of the task. While the signal associated with coronary artery disease clearly manifests itself as higher frequency energy, the general consensus in literature is that the previously discussed experimental and theoretical studies have shown that the signal is too variable and too faint for any of the feature-detection based techniques attempted to date to accurately detect the signal under the noisy conditions of the chest. It is appropriate here to repeat the thoughts of Semmlow, who was one of the pioneers of the field. Rather than paraphrase and dilute the meaning, instead I quote directly from the conclusions from his recent review article[7]:

> *"Considerable work has been directed toward fulfilling the promise of detecting CAD from heart sounds recorded at the chest. The problem is essentially one of resolving a very faint signal buried in a substantial amount of noise. Many powerful signal processing techniques address this type of signal-to-noise problem, but they require some a priori knowledge about the signal characteristics. Unfortunately, little is known about the signal produced by blocked coronary arteries. Modeling and mathematical studies on idealized blockages where a continuous flow flows through a fixed blockage in a straight tube suggest the signal will be narrowband as a result of resonances in tube walls. The success of spectrally based methods suggests that this assumption must be at least partially true. However, coronary blood flow is highly variable, even more so than in other arteries, owing to the continuous changes in vessel wall tension. Moreover, the arteries themselves undergo a variety of contortions as the surface of the heart moves during contraction and relaxation. Finally, the blockages themselves are often diffuse and distributed over a section of artery. Thus, it is unlikely that the signal generated by coronary blockages is a simple narrowband signal, but in many patients, it is distributed over a range of frequencies following complex timing. Improving on results described above will likely require searching for quite different features than those outlined above" (Emphasis mine)*
>
> *-John Semmlow & Ketaki Rahalkar, 2007*

This passage states in no uncertain terms that despite the results contained in the literature described previously (much of which was performed by Semmlow and colleagues) applying feature detection to diastolic sounds to detect CAD remains uncertain an uncertain affair. In contrast, the fundamental concept behind the beamforming and acoustic imaging approaches is sound. If one knows the spatial location of sound sources within the chest, one can examine the sounds emitted solely from the coronary arteries, and exact knowledge of the spectral characteristics is no longer very important – a noisy artery is most likely an unhealthy artery. This would represent sufficient evidence to justify more determinate tests, such as convention angiography. Unfortunately, such techniques are limited by the fact that the size of the chest is too small compared to the applicable wavelengths for such techniques to be effective. The size of the chest is on the order of a single meter, while the wavelength of sound in water (which has similar acoustic properties to soft tissue), even at 1000 Hz, is 1.5 m. This places the entire chest within the nearfield, where such techniques perform poorly, if at all.

Nevertheless, the promise offered by a technique that could separate sources based upon their location is hard to ignore, particularly in light of the failings of feature-based detection. This promise provides the motivation for this work. In the first portion of this chapter, a novel approach to phonoangiographic signal processing is discussed. This approach is based upon separation of signals based upon knowledge of the acoustic transfer within the chest. Hence, the fundamental questions regarding the validity of the technique involve the similarity of acoustic transfer functions between different source locations within the chest and sensor locations on the chest surface. To answer these questions, finite element modeling of a physiologically accurate human chest geometry was performed. The development of this finite element model, as well as the matrix algebra tools used to analyze the finite element model are discussed in the later portions of this chapter, the results from the model are saved for chapter 3.

2.2. PROPOSED TECHNIQUE

The proposed approach relies fundamentally upon the observation that the amplitudes of sound waves within the chest are sufficiently small so that they can be treated with the theory of linear acoustics. Fortunately, the sounds emitted by the circulatory and respiratory systems are sufficiently small that this is indeed the case. As a result, the signal reaching the skin surface from an acoustic point source located at some location within the chest can be represented using a transfer function H_{ij}, which is a function of frequency:

$$H(\omega)_{ij} = \frac{v(\omega)_i}{s(\omega)_j} \qquad \text{Eq. 2-1}$$

where v_i represents the acoustic particle velocity encountered at the i^{th} location on the chest surface. Similarly, s_j represents the particle velocity associated with the j^{th} acoustic point source located inside the chest. Note that an acoustic point source is defined as a small (but finite) cylinder (2-D) or sphere (3-D) which is vibrating radially[60]. A further description of acoustic point sources appears in Appendix A. The particle velocity of the source is defined as the radial velocity of this cylinder of sphere so that each value H_{ij} is a unitless ratio. ω represents angular frequency. In acoustics, a distributed acoustic source can represented by a series of acoustic point sources[60]. This leads to the observation that all sounds within the chest can be thought of as being generated by some number of point sources, distributed throughout the chest.

Since we are within the realm of linear acoustics, in the frequency domain the velocity at any given surface location can be calculated using a linear system of equations:

$$\mathbf{H}(\omega)\mathbf{s}(\omega) = \mathbf{v}(\omega) \qquad \text{Eq. 2-2}$$

where H is a m x n matrix, where m represents the number of surface locations, and n represents the number of point sources modeled within the chest; this matrix will henceforth be known as a mixing matrix. **s** represents a n x 1 column vector, corresponding to the amplitude of the particle velocity of each acoustic source, and **v** represents a m x 1 column vector, corresponding to the amplitude of the particle velocity at each surface location. However, in a clinical scenario, the variable of interest is not the surface velocity, **v** (which can be measured), but rather the source strengths, **s**. Note that this system in general is not square ($m \neq n$), so that the solution is not strictly speaking invertible, and cannot be solved using the normal methods of linear algebra (LU-decomposition, matrix inversion, Gaussian elimination, etc.).

However, a best fit solution to this matrix can be obtained through the process of pseudoinversion, which is essentially a least squares equivalent to the inversion of a square matrix. Whereas matrix inversion provides the solution to a square system of linear equations, pseudoinversion provides the best fit solution to the solution of an over- or under-determined system of linear equations. Applying pseudoinversion to the linear system described by equations 2.2, one obtains:

$$\mathbf{s}(\omega) = \mathbf{W}(\omega)\mathbf{v}(\omega) \qquad \text{Eq. 2-3}$$

where matrix *W* represents the pseudoinverse of the mixing matrix *H*, and is known henceforth as the demixing matrix. As a result, with knowledge of the demixing matrix *W*, and measurements of the surface velocity, **v**, it is possible to estimate the acoustic source strength at each point source location for which a set of transfer functions exists.

This pseudoinverse can be obtained by performing a singular value decomposition of the mixing matrix *H*. The singular value decomposition of *H* can be represented by:

$$\mathbf{H} = \mathbf{U}\Sigma\mathbf{V}^{*} \qquad \text{Eq. 2-4}$$

where matrix *U* is an *m*-by-*m* unitary matrix, Σ is an *m*-by-*n* diagonal matrix where the terms on the diagonal are the singular values of *H*, and *V** is the conjugate transpose of *V*, which is a *n*-by-*n* unitary

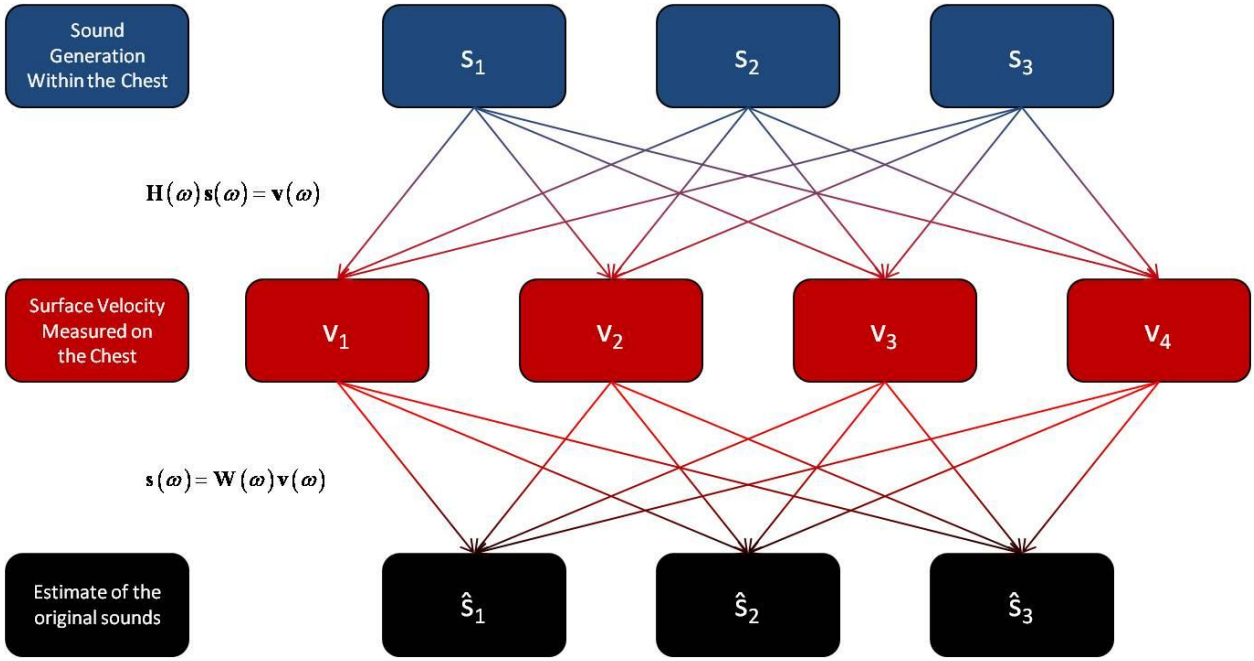

Figure 2-1: Graphical representation of the proposed source separation. In the physical system, acoustic sources within the chest generate sounds which propagate out and cause the chest surface to vibrate. To estimate the source strengths based upon surface measurements, the pseudoinverse of the mixing matrix is multiplied by the surface measurements.

matrix. Note that if the values of *V** are purely real, this is simply the transpose. After performing the singular value decomposition, the pseudoinverse *W* can be calculated by:

$$\mathbf{W} = \mathbf{V}\boldsymbol{\Sigma}^{-1}\mathbf{U}^{*} \qquad \text{Eq. 2-5}$$

Once this pseudoinverse has been obtained, the source signals can be estimated using equation 2.3. The overall algorithm is represented graphically in Figure 2-1.

2.3. Finite Element Model Development

As previously described, the proposed technique depends heavily upon the ability to practically invert the acoustic transfer matrix of the chest, and a major portion of this work involves calculation of the matrix condition number of this matrix at different frequencies. Clearly, such an analysis requires knowledge of the acoustic transfer within the chest. A 2-D finite element model of the chest was developed to obtain such information using ANSYS 11.0 (ANSYS, Inc., Canonsburg, PA). An overview of the process used to develop this model is shown in Figure 2-3; a discussion of this process follows. The 2-D geometry for the model was obtained from the Visible Human Project Server, supported by École Polytechnique Fédérale de Lausanne, which has published cryosection images of an entire human body. The cryosection image utilized in this study, shown in

Figure 2-2, represents a transverse slice of the chest geometry passing through the chest at a level corresponding to the most common site of occlusion of the main left coronary artery. This represents the 'worst-case scenario for the occurrence of a coronary blockage, and the prognosis for such an event is sufficiently poor as to be commonly referred to as the 'widowmaker'. The geometry for the model was obtained by manually fitting splines to the interfaces between different tissue types appearing in the cryosection image, which was performed in SolidWorks (Dassault Systèmes SolidWorks Corp., Concord, MA). In this step, four different regions were identified:

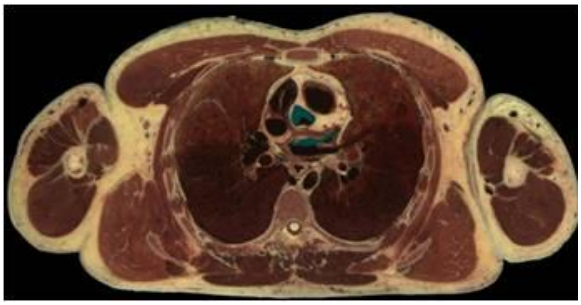

Figure 2-2: Transverse cryosection image obtained from the École Polytechnique Fédérale de Lausanne Visible Human Project Server. The axial location of this slice within the chest corresponds to the most common location for the occurence of main left coronary artery occlusions

1) Soft tissue (muscle, skin, fat, etc.)
2) Bone
3) Air
4) Blood

Additionally, both internal and external free surfaces were identified and marked in this step (internal free surfaces occur in the right and left primary bronchi, which carry air to the lungs). Using these splines, areas representing like materials were defined, resulting in a surface geometry which was imported into ANSYS, where it was meshed and material properties were assigned.

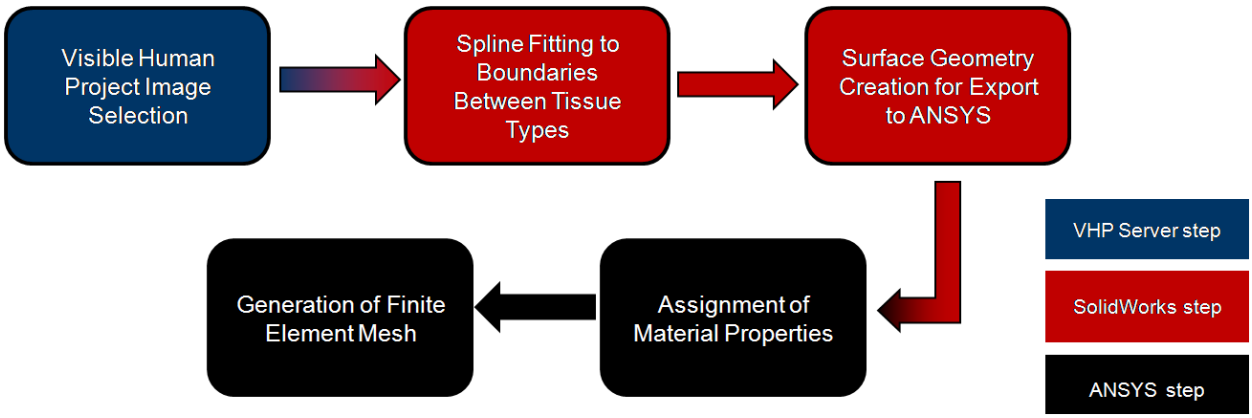

Figure 2-3: Overview of the process used to build the finite element model. The model geometry was obtained from a cryosection created by the Visible Human Project. A CAD geometry was created based upon this image was created by fitting splines to the boundaries between tissue layers in the image. The resulting CAD geometry was exported to ANSYS where the finite element model was built by meshing the imported geometry.

2.4. Material Properties and Mesh Generation

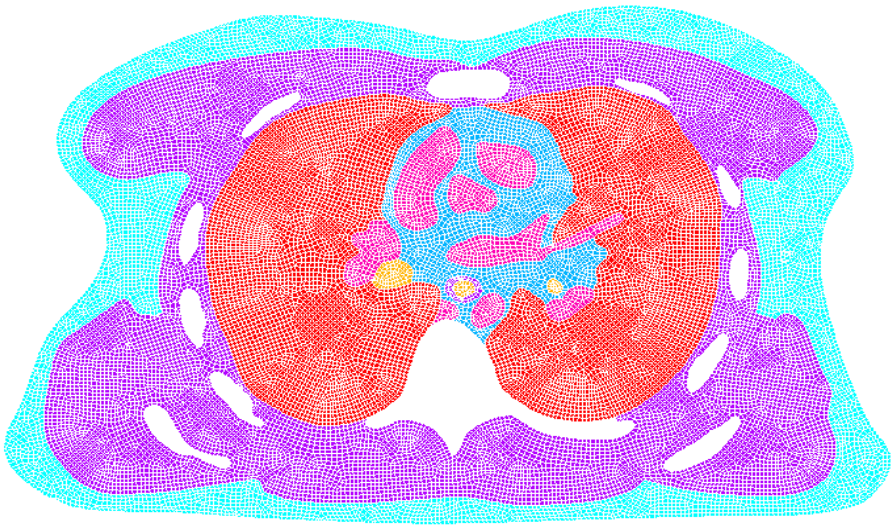

Figure 2-4: Initial mesh produced from the cryosection geometry. Teal regions correspond to skin and sub-cutaneous fat. Purple regions correspond to muscle, while light blue regions correspond to cardiac muscle. Red regions correspond to lung parenchyma, while yellow regions correspond to internal air. Finally, magneta regions correspond to blood. Note that the unmeshed 'holes' in the model (appearing white) correspond to bony regions. Elements bordering such holes were assigned rigid boundary conditions. All soft tissue was assigned identical material properties.

Four different tissue types were identified during the previous spline fitting step. Both soft tissue and blood were assigned material properties corresponding to those of water. Bone was assumed to be

acoustically rigid, and thus was not meshed, but instead a fixed boundary condition was applied at the interface of soft tissue with bone. Finally, lung parenchyma was assigned material properties identical to those used in the analyses of Royston et al. and Mansy et al., who studied the propagation of sounds within the chest with the aim of acoustically detecting the presence of pneumothorax[61, 62]. The use of material properties of water to represent soft tissue and blood also follows the analyses of Royston et al. and Mansy et al. The assigned acoustic properties are summarized below in Table 2-1. Air is treated two separate ways in this model. Internal air pockets are meshed within the model, while external air is accounted for by applying a pressure release (P=0) boundary condition.

The geometry was meshed using ANSYS FLUID29 elements. These elements are linear quadrilaterals developed through discretization of the 2-D wave equation. It is important to note that this element does not possess the capability to model dissipative (viscoelastic) materials. Thus, it was model necessarily assumes that elastic behavior (alternatively, that the speed of sound is purely real) and that the model is undamped. The importance of this assumption will be discussed later. Where necessary, reduced triangular versions of these elements were used to generate valid meshes, however, very few (less than one percent) such elements exist in the final mesh. A maximum element size of less than 1 mm was used in the initial mesh. This initial mesh is shown in Figure 2-4.

Tissue Type	Speed of Sound (m/s)	Density (kg/m^3)
Bone	-- (modeled as rigid)	-- (modeled as rigid)
Soft Tissue (muscle, skin, etc)	1500	1000
Blood	1500	1000
Lung Parenchyma	30	300

Table 2-1: Material properties assigned to each tissue type represented in the finite element model. Note that the material properties assigned to both soft tissue and blood are identical to those of water. These values are consistent with those used in the previous acoustic analyses of Royston et al. and Mansy et al.[61, 62]

2.5. MESH VALIDATION

As previously discussed a necessary assumption made in the development of the model was that the behavior of the elements is strictly elastic. This assumption leads to a significant limitation of model. It is a well known result in vibration theory that driving a purely elastic model near a resonant frequency leads to infinite harmonic response. Thus, as the driving frequency approaches a resonant frequency, the behavior of this finite element model can be expected to trend towards infinity. In reality, the behavior near such frequencies is limited by the viscoelastic properties of the model, but, these properties have been neglected. Because driving the model near resonance does not affect the shape of the response, this assumption is acceptable when comparing the acoustic transfer functions, which depends upon the excited mode shapes. However, it makes validation of the mesh more difficult, since the actual response of the model is extremely sensitive to the mesh.

As a result, the resonant frequencies of the model (as determined by modal analysis) were used as system response quantities for mesh validation. The mesh was assumed to acceptable if the resonant frequencies converged asymptotically, since this indicates that the mesh is sufficiently fine that the errors involved in computation are decreasing with mesh size as would be predicted theoretically by the order of the elements and the degree of mesh refinement. To demonstrate that the mesh does indeed exhibit such behavior, two systematic refinements of the mesh were performed, each halving the mean element length,

with resonant frequencies being calculated for the initial mesh as well as both refinements. An additional benefit of this approach is that it allowed explicit, independent examination of the validity of the mesh at different frequencies, since there are a large number of resonant frequencies within the frequency range of interest.

To confirm that the mesh size is sufficiently small for asymptotic reduction in model errors, the observed order of convergence of the series of meshes was calculated using the resonant frequencies calculated for each of the three previously described meshes. According to Roache, the observed order of convergence can be calculated by[63]:

$$p_k = \frac{\ln\left(\frac{f_{k,0} - f_{k,1}}{f_{k,1} - f_{k,2}}\right)}{\ln(r)} \qquad \text{Eq. 2-6}$$

where p_k represents the order of convergence calculated using the kth resonant frequency. $f_{k,i}$ represents the value of the kth resonant frequency calculated using the ith iteration of mesh refinement. Hence, i=0 refers to the initial mesh, while i=1 and i=2 refer to the meshes produced by the 1st and 2nd iterations of mesh refinement, respectfully. Finally, r represents the ratio of the previous (parent) mesh to the refined mesh. Since in this study the length of elements were approximately halved each iteration of mesh refinement, r=2.

The results from applying Eq. 2 6 to the resonant frequency calculations from each mesh are shown in Figure 2 5. The expected, theoretical order of accuracy of the solution for the resonant frequencies is p=2. Inspection of the results shows fairly good agreement between the theoretical and observed orders of accuracy at lower frequencies, and exceptional agreement at higher frequencies. Since such agreement can be observed only if all three of the meshes used in the calculation are sufficiently fine so as to have

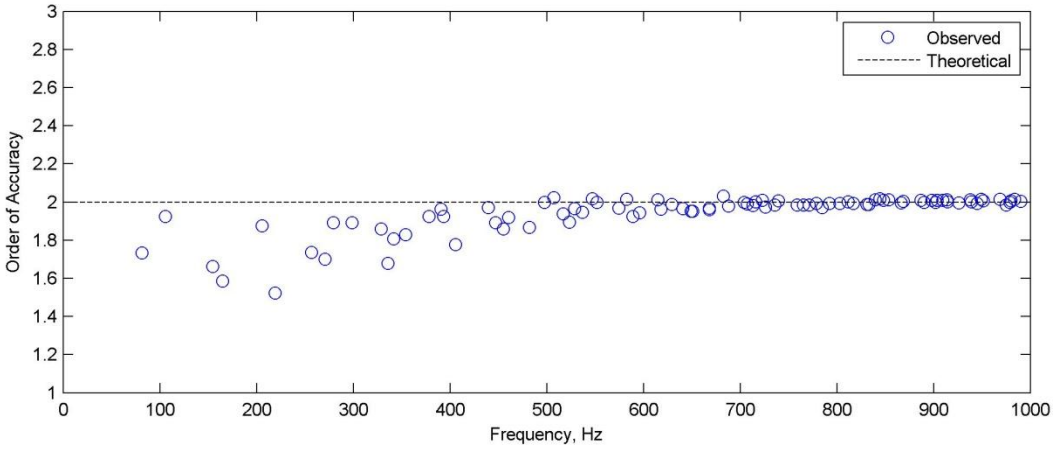

Figure 2-5: Comparison of the theoretical and observed orders of convergence from the mesh verification study. These results show good agreement in the lower portion of the frequency range of interest, and exceptional agreement at the higher end of the frequency range. As a result, it can be concluded that the initial mesh is sufficiently fine to possess asymptotic error behavior, and is suitable for use in calculations

asymptotic error behavior, it can be concluded that the initial, coarse mesh is sufficiently fine so as to possess asymptotic behavior. This means that the results are within a well-defined error (which decreases asymptotically with increasing mesh size) of the true solution, and that the mesh is sufficiently to produce reliable results within the range of this error.

2.6. TRANSFER FUNCTION CALCULATION

In this study, fourteen separate acoustic point sources were applied to the previously described and validated finite element model. The locations of these point sources appear in Figure 2-6, and descriptions of their locations appear in Table 2-2. Although the use of fourteen source locations is almost certainly insufficient for clinical use of the technique, it is a sufficient number of point sources to examine the variation of acoustic transfer functions originating from different locations within the chest. To calculate transfer functions, a point source of unit amplitude was applied to the node corresponding to the point source location. This was implemented in ANSYS using the FLOW load command. The harmonic solutions of the model were then produced over a range of 0-800 Hz, with frequency steps of .66 Hz. An overview of this process is shown in According to the definition of an acoustic transfer function presented in Eq. 2-1, the transfer function between the current point source and a given surface node is simple equal to the calculated response of the node, since the point source is of unit strength. Transfer functions were calculated for each surface node present in the mesh, and were used to assemble the acoustic transfer function matrix $H(\omega)$, as described in the previous theory portion of this chapter.

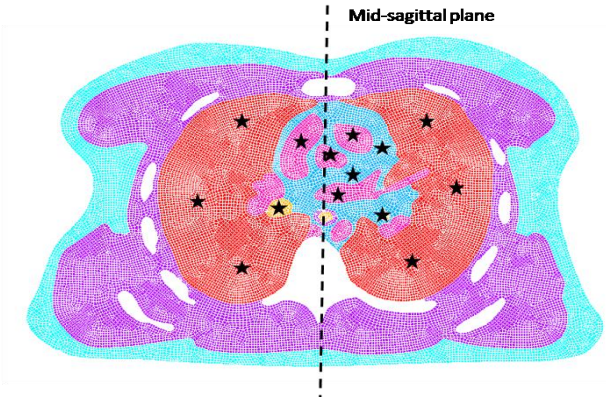

Figure 2-6: Locations of the point sources for which transfer functions were calculated. Fourteen different point sources were considered. Transfer functions were calculated between each source location and each surface node

Point Source Locations	
Left Coronary Artery	*Left Primary Bronchus*
Right Coronary Artery	*Right Ventral Lung*
Right Ventricle	*Right Mid-Lung*
Right Atrium	*Right Dorsal Lung*
Left Atrium	*Left Ventral Lung*
Descending Aorta	*Left Mid-Lung*
Right Primary Bronchus	*Left Dorsal Lung*

Table 2-2: Positions of the point source locations for which transfer functions were calculated. Note that the transfer function between each listed source location and all surface nodes was calculated. Descriptions in italics represent point sources associated with the respiratory system, as opposed to the cardiovascular system

2.7. MATRIX CONDITION NUMBER & ERROR PROPAGATION CALCULATIONS

As previously shown with Eq. 2-2 and Eq. 2-3, the proposed technique depends heavily upon the inversion of the acoustic transfer matrix $H(\omega)$. Much of the vulnerability of this technique to measurement error depends heavily upon how easily this matrix can be numerically inverted, as defined by the matrix condition number, k. A low matrix condition number corresponds to a well conditioned system of equations, which is easily invertible. With such a system, errors in the forcing vector produce only small errors in the solution. In the context of the current work, if the condition number of the acoustic transfer matrix $H(\omega)$ is small, then errors occurring in the measurement of the surface velocity will produce only small errors in the estimates of the amplitudes of internal sources. Conversely, if the matrix condition number of the system is large, then the technique is susceptible to measurement errors, and even small errors in surface velocity measurements may produce large errors in the estimated source

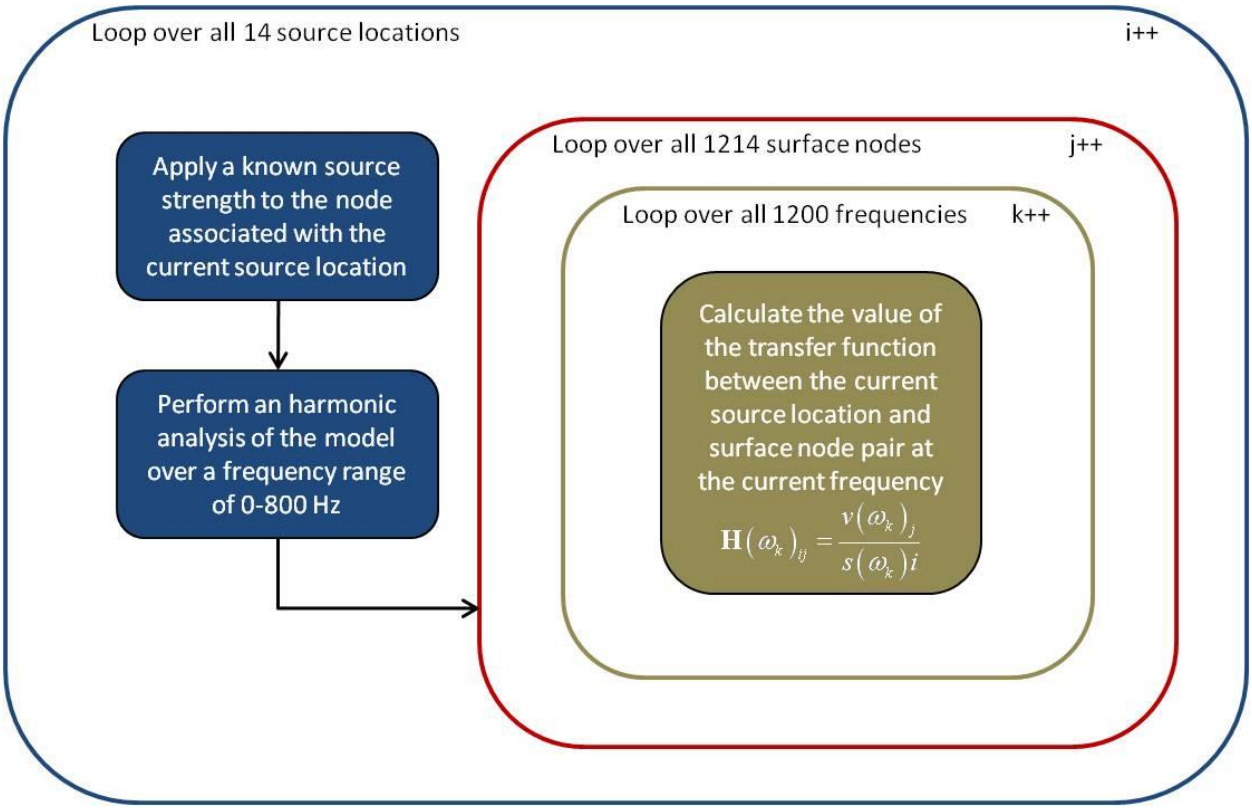

Figure 2-7: Overview of the process undertaken to calculate the transfer functions of each source location. An outer loop looped over the 14 source locations within the chest. A point source of unit strength was applied at this location, and the model was solved, sweeping over a frequency range of 0-800 Hz. After having solved the model, another loop recorded both components of the surface velocity at each node on the outside of the model. Once this surface velocity has been retrieved, the value of the transfer function between the i^{th} source location and the j^{th} surface node at the k^{th} frequency can be calculated by dividing the the surface velocity by the source strength. A total of 8498 transfer functions were calculated. Note that hollow (unfilled) boxes indicate for loops, while filled boxes indicate steps taken within the loop. The variable in the upper right hand corner of the loop is the index variable for the loop.

strengths. As a result, the matrix condition number of the acoustic transfer functions of the chest represents a major interest throughout this work.

The condition number of a matrix is calculated by taking the product of the operator norms of a matrix and its inverse:

$$k(\mathbf{A}) = \|\mathbf{A}\|\|\mathbf{A}^{-1}\| \qquad \text{Eq. 2-7}$$

Because there are multiple operator norms, there are multiple different definitions of the condition number. In the case of this work, the decision was made to use the ℓ-2 operator norm, in which case the matrix condition number can be calculated by taking the ratio of the maximum and minimum singular values of the acoustic transfer matrix, *H(ω)*:

$$k(\mathbf{A}) = \frac{\max(\Sigma)}{\min(\Sigma)} \qquad \text{Eq. 2-8}$$

Note that this definition guarantees that the minimum possible value of the matrix condition number is 1. The mathematical significance the condition number of a matrix is that it supplies a bound on the propagation of error that occurs when solving a linear system of algebraic equations. The error in the solution to the system is governed by the inequality[64]:

$$\delta s \le k(\delta H + \delta v) \qquad \text{Eq. 2-9}$$

where δs, δH, and δv represent the relative errors present in the source strength vector, the transfer function matrix, and the surface velocity vector. The relative error of a vector or matrix is defined as:

$$\delta s = \frac{\|\mathbf{s} - \hat{\mathbf{s}}\|}{\|\mathbf{s}\|} \qquad \text{Eq. 2-10}$$

where $\hat{\mathbf{s}}$ represents the approximate vector contaminated with error. From Eq. 2-9 it is apparent that while the condition numbers does not tell us what there is, it does give us a threshold which the error will be below. More formally, the matrix condition number bounds the norm of the relative error in the solution. In this work, however, one further step was taken, and a series of numerical experiments was performed to estimate the amplification of the error which occur in solving the system. At each frequency, a set of arbitrary source strength vectors was generated, which were then used to calculate an exact vector of surface velocities, using the already calculated transfer functions, according to Eq. 2-2. This velocity vector was then contaminated with random error. This was done with errors on the order of 10^{-11} through 10^{-3}. Forty iterations were performed at each level of error. In each iteration, Eq. 2-3 was used to calculate an estimate of the source strength vector based upon the contaminated velocity vector. Relative errors were calculated for both the contaminated source strength vector, $\hat{\mathbf{s}}$ and the contaminated surface velocity vector, $\hat{\mathbf{v}}$. The results from each simulation were then used to fit a linear relationship between the amount of error present in the surface velocity vector, and the mean error present in the source strength vector:

$$\delta s = \beta \delta v \qquad \text{Eq. 2-11}$$

The fitted constant β, henceforth referred to as the error amplification factor represents the average amount by which errors in the surface velocity vector are increased in the resulting estimate of source strength vector. This error amplification factor can be thought of as an estimate of the actual value of the quantity which the matrix condition number bounds.

3. NUMERICAL RESULTS & DISCUSSION

3.1. TRANSFER FUNCTIONS & IMPLICATIONS FOR FEATURE DETECTION

As discussed previously in Section 2.6, transfer functions were calculated between each of fourteen different acoustic source locations within the chest, and the full set of surface nodes. The resulting sets of transfer functions for the left and right coronary arteries are shown in Figure 3-1 and Figure 3-2. Similar plots can be produced for the other source locations listed in Table 2-2, however, for brevity, most of these results are shown in Appendix B. Several important observations can be made immediately from examination of the transfer functions for the left coronary artery. First, this data clearly confirms that any signal associated with CAD reaching the skin surface will be extremely faint, subject to signal losses at least on the order of -100 to -200 dB. Additionally, this data suggests that resonant frequencies of the chest populate the entire frequency range which is of interest in phonoangiography. This suggests that the use of spectral feature detection algorithms will have to overcome an additional problem on top of those discussed previously. Specifically, the acoustic transfer functions of the chest will act as a very complicated filter, which will act upon the CAD signal before it is ever received by sensors located on the skin surface, thus distorting the spectra before it is ever recorded by a microphone. As discussed earlier, many research studies have performed animal or benchtop experiments, where microphones could be placed near the artery, and this affect was not significant. However, the primary advantage of phonoangiography remains its potential for noninvasive detection. Noninvasive detection requires that sensors be placed on the skin surface; as a result, the described affect is a significant one that conventional techniques would have to overcome.

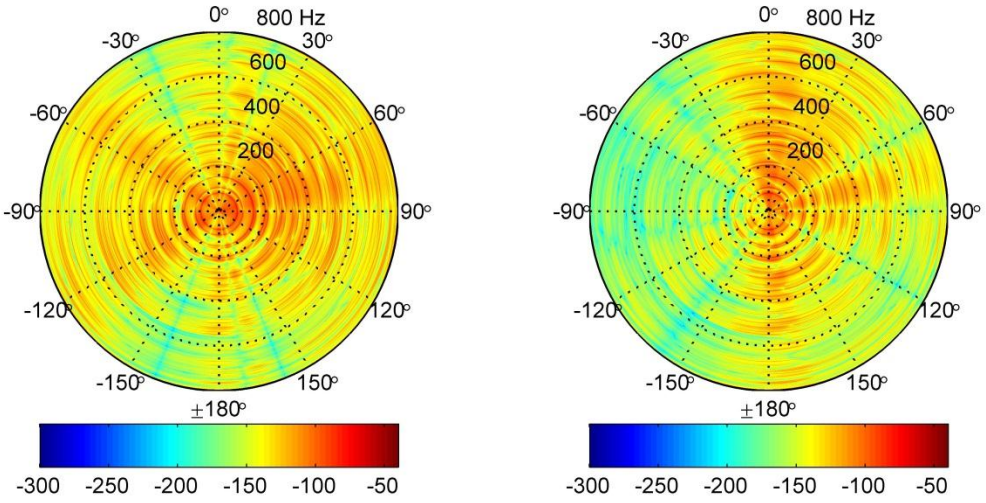

Figure 3-1: *left:* x-velocity component acoustic transfer function corresponding to a point source located in the left coronary artery. *right:* acoustic transfer function for the y-component of velocity. Radial coordinate corresponds to frequency, while the angle coordinate corresponds to surface position, measured by angle from the anterior mid-sagittal plane. Colorbar units: dB.

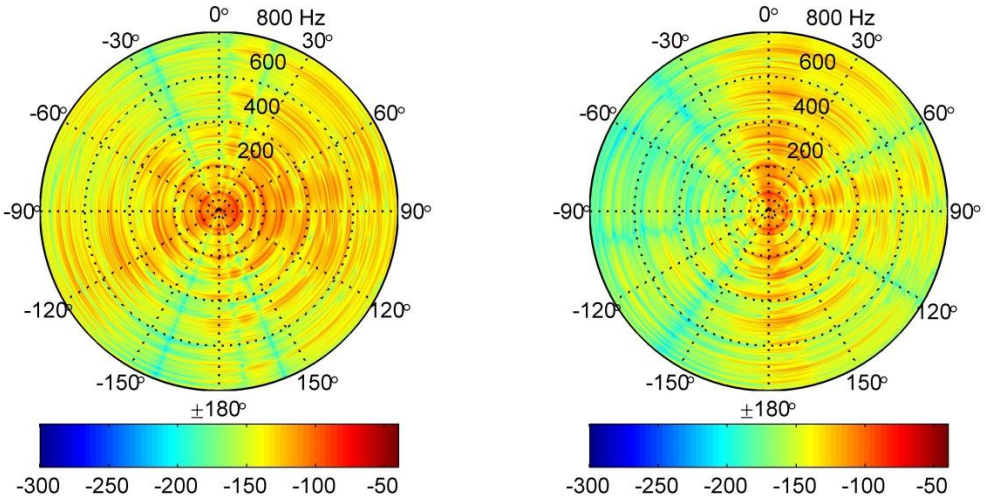

Figure 3-2: *left:* x-velocity component acoustic transfer function corresponding to a point source located in the right coronary artery. *right:* acoustic transfer function for the y-component of velocity. Radial coordinate corresponds to frequency, while the angle coordinate corresponds to surface position, measured by angle from the anterior mid-sagittal plane. Colorbar units: dB.

Of more interest to the current technique, is the spatial variation of the acoustic response along the chest surface and the variation between the responses corresponding to different source locations. Here, both good and bad news is encountered. Inspection of results in both Figure 3-1 and Figure 3-2 show that surface response depends heavily upon the location on the chest. The observed pattern is one of regions of high response, separated by narrow regions of low response. The existence of this variation is excellent news for the proposed algorithm, since it suggests that microphones located at different locations on the chest will hear very different signals. However, the results presented in Figure 3-1 and Figure 3-2 can give little physical insight into why this pattern arises, since these figures present only the surface response.

To explain this pattern, the acoustic field inside the chest is examined. Recall that the results in Figure 3-1 and Figure 3-2 are only from the skin surface. Figure 3-3 shows the magnitude of the particle velocity field inside the chest, resulting from a point source located in the left coronary artery oscillating at 50 Hz. Note that this frequency was chosen somewhat arbitrarily – there is nothing particularly special about 50 Hz, but it is not practical to plot the internal field throughout the frequency spectrum. Examination of these internal fields leads to the conclusion the pattern observed on the chest surface is due to the interaction of the acoustic field with the bony structures of the chest, especially the rib cage. These bony structures reflect incident sounds waves, leading to acoustically shadowed regions on the skin surface behind the structure.

Although there is large variation in response at different locations on the chest, variation between different sources appears to be much more modest. Examination of Figure 3-1 and Figure 3-2 shows that although differences in the two sets of transfer functions do exist, there is also a great deal of similarity as well. To some extend this is expected, since the right and left coronary artery are relatively close together

in their anatomical position. For comparison, Figure 3-4 shows the same transfer functions for the left dorsal lung, which is located in a much more dorsal position than the coronary arteries, as well as off to one side. Comparison of these transfer functions with those corresponding to the left and right coronary arteries reveals that even in the case of further removed source locations, a great deal of similarity remains in the acoustic transfer functions. This suggests that the acoustic transfer function matrix may represent a poorly conditioned system of equations, which would lead to the algorithm being vulnerable to inevitable errors in the measurement of surface velocities.

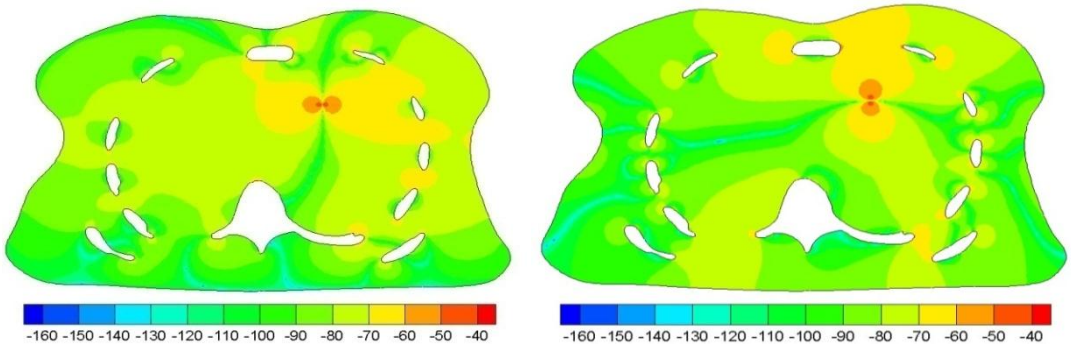

Figure 3-3: Internal acoustic particle velocity field resulting from an acoustic point source oscillating at 50 Hz located within the left coronary artery. These results suggest that the interaction of the acoustic field with the ribs leads to shadowed regions of low surface response of the chest surface.

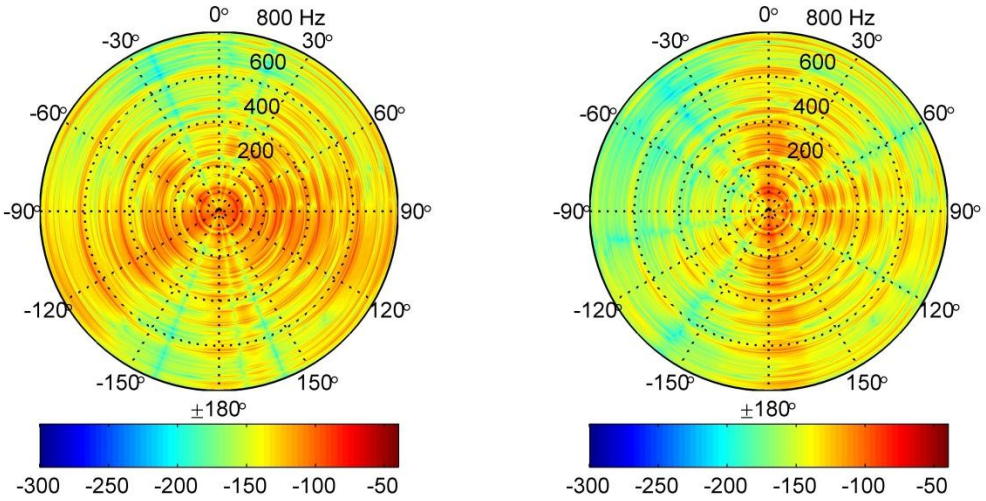

Figure 3-4: *left:* x-velocity component acoustic transfer function corresponding to a point source located in the left dorsal lung. *right:* acoustic transfer function for the y-component of velocity. Radial coordinate corresponds to frequency, while the angle coordinate corresponds to surface position, measured by angle from the anterior mid-sagittal plane. Colorbar units: dB.

3.2. MATRIX CONDITION NUMBERS & SOURCE SEPARATION RESULTS

Before examining the matrix condition numbers of the acoustic transfer matrix, the ability of the proposed approach to detect CAD in a numerical environment lacking measurement errors but possessing high levels of background noise is considered. Towards this end, data vectors corresponding to random noise were created for each of the fourteen point sources considered in the study (listed in Table 2-2). The RMS values of the vectors corresponding to the left and right coronary arteries were one thousand times less than those applied to the remaining twelve sources, so as to simulate the much weaker signals emitted by these arteries. The Fourier transforms of these data vectors were taken, and used to apply source strengths

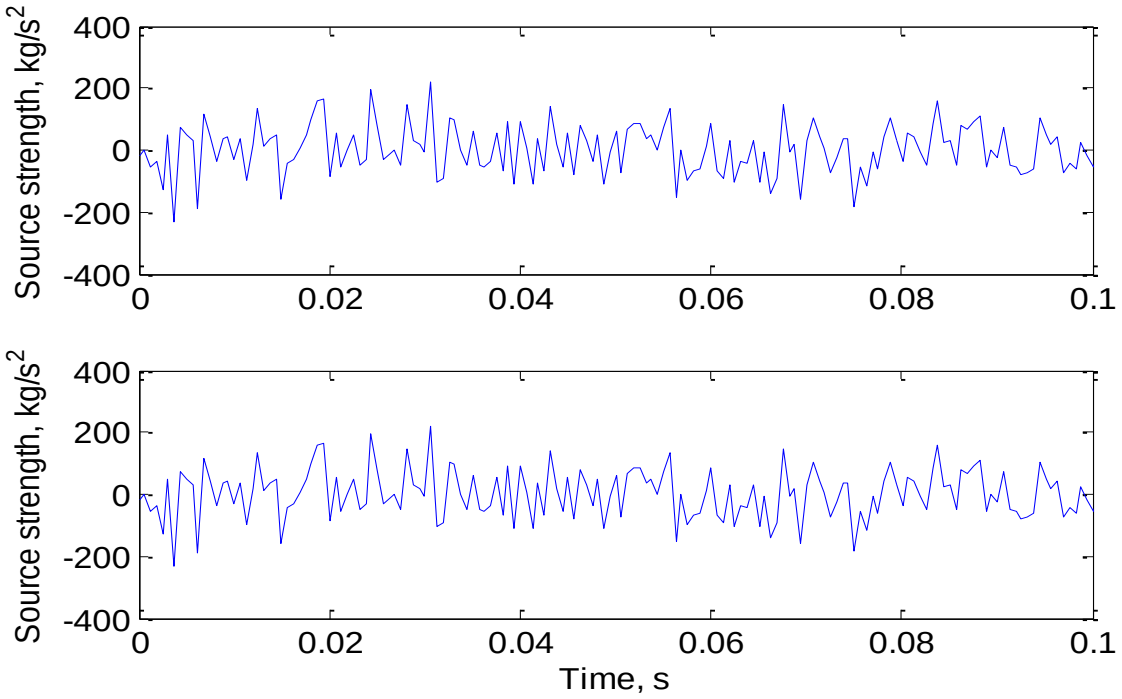

Figure 3-5: True and estimated source strength time series for the left coronary artery, produced in the previously described test case without measurement error but in a noisy environment. *Top:* Actual signal input into the source *Bottom:* Estimate of the source strength time series produced by applying the proposed algorithm to the surface velocity data. These results clearly demonstrate the effectiveness of the technique in the absence of measurement error.

to the point sources in the finite element model. The frequency spectrum of the surface response of each node was then obtained by performing a harmonic analysis in ANSYS, sweeping the entire frequency range of 0-800 Hz.

The results from this test case are shown in Figure 3-5. Inspection of these results reveals excellent agreement the true input signal and the estimate calculated from the surface velocity spectra. This demonstrates the ability of the technique to separate the sounds coming from an individual source location, based upon knowledge of the acoustic transfer functions. The test case also demonstrates the immunity of the technique to background noise, since this test case was performed in the presence of many background noise sources whose RMS strength was orders of magnitude greater than the source located at the left coronary artery. However, these results say nothing about the vulnerability of the

proposed technique to measurement errors, which is examined through the calculation of matrix condition numbers and the propagation of errors.

3.3. MATRIX CONDITION NUMBERS & ERROR PROPAGATION

The approach used in this study for the calculation of matrix condition numbers is described in Section 2.7. Condition numbers were calculated for the acoustic transfer matrix at each frequency for which transfer functions were calculated. The resulting condition numbers are shown in Figure 3-6. As a brief reminder, this metric measures the propagation of error that occurs in solving a linear system of equations

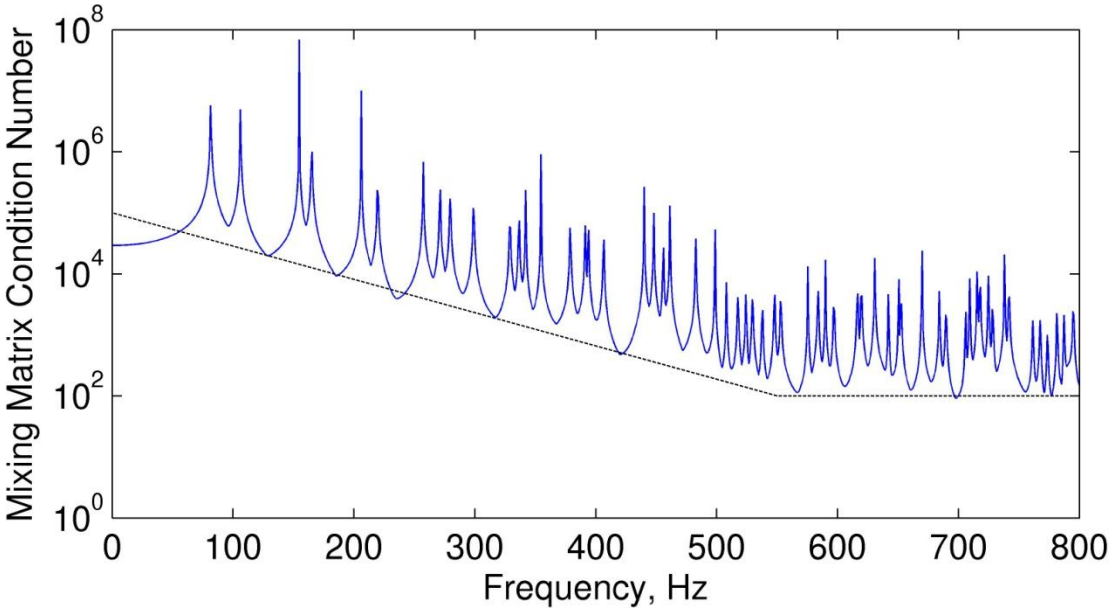

Figure 3-6: Condition numbers of the acoustic transfer function matrix over a frequency range of 0-800 Hz. The condition numbers of the matrix are prohibitively high at lower frequencies, but reduce to more manageable levels for frequencies above 550 Hz. The peaks present in the data correspond to the resonant frequencies of the model. The black line corresponds to a trendline, which looks at the error propagation outside of the resonance spikes.

through inversion of the coefficient matrix. The high condition numbers observed at lower frequencies suggest that in that frequency range the proposed technique is not practical. In contrast, the results show that these condition numbers level off to about k=100 for frequencies above 550 Hz. Thus, while the system is still sensitive to numerical errors, this affect is significantly reduced in this higher frequency range.

These results strongly suggest that the proposed technique is most likely be to be effective if the sounds associated with CAD have strong components at frequencies greater than 550 Hz. For a more intuitive representation of the sensitivity of the system to measurement error, the propagation of errors through the system were calculated, according to the procedure described in Section 2.7. The resulting error amplification factors are shown in Figure 3-7. The same trends are observed in these results as were observed in the condition numbers shown in Figure 3-6, with extremely low error tolerance and very large amplification of errors at low frequencies, but with manageable levels at frequencies above 550 Hz. Note that these error amplification factors, especially above 550 Hz, tend to be at least an order of magnitude

less than the matrix condition number. Thus, on average the error propagation through the system tends to be about an order of magnitude better than the theoretical worst case.

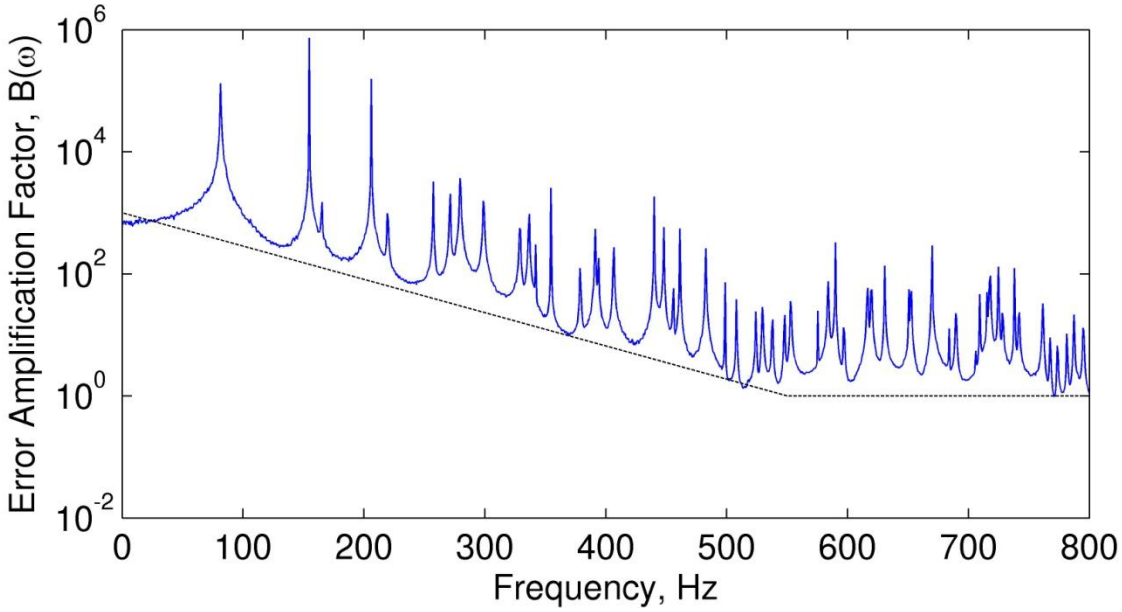

Figure 3-7: Error amplification factors representing the average propagation of error through the system. The same trends are observed in this data as are observed in matrix condition numbers shown in Figure 3-6, with high amplification of the error at lower frequencies, but much more manageable increases in the error at frequencies above 550 Hz. Note that the actual behavior of the system is rather more forgiving than the theoretical limit. Above 550 Hz, the amplification of the errors tends to be on the order of 10, while the matrix condition numbers are on the order of 100. Thus, the actual error tolerance of the system is on average about an order of magnitude better than the theoretical limit.

3.4. Discussion & Future Work

The results shown in the previous subsections have demonstrated the ability of the approach described in Section 2.2 to separate the acoustic signals produced by stenosed coronary arteries from the background noises in the chest based upon the differences in the acoustic transfer functions from each source location. However, the matrix condition numbers (which represent a theoretical limit on the levels of error) and the error propagation factors (which represent the actual average errors encountered) results shown in Figure 3-6 and Figure 3-7 show that at frequencies below 550 Hz the technique has severe issues with tolerance of errors in the measurement of the surface velocities. At frequencies near or above 550 Hz, these errors are manageable. This leads directly to the observation that the usefulness of the technique is heavily dependent upon the actual frequencies of the CAD associated sounds which the technique is attempting to detect. If the spectral content of these sounds is below this threshold frequency the proposed source separation breaks down; above this frequency it is quite feasible.

Examination of the prior work in this area, discussed previously in Section 1.4, and summarized in Table 1-1, reveals an uncertain picture. While many of these studies have shown frequencies for which the proposed technique is feasible, others reported sounds at lower frequencies, between 100 and 200 Hz, for which technique is impractical. There is an observed trend that the more recent studies, which have used more sophisticated signal processing algorithms intended for stationary signals such as those associated

with CAD, have tended to predicted content at higher frequencies. Most notable here are the STFT results of Mohler[41], which predicted frequencies at around 800 Hz. However, there is still much uncertainty with regard to actual characteristics of the sounds associated with CAD, which, as discussed previously is one of the main motivations for the approach taken in this work. This presents the first of several avenues for future work in this area. There is a great need in this area for rigorous, benchtop experiments (where more factors can be controlled) which examine the sounds produced by stenosed arteries with complicated cross sections in pulsatile flow, rather than merely studying axisymmetric cross sections. Additionally, the structural properties of the vessel should be varied in these experiments. The acoustic recordings obtained in the proposed experiments should be coupled with hydrodynamic and structural measurements, to gain insight into the exact mechanisms producing the sound under different circumstances. Such data would both give the community a better idea of the expected frequencies of interest, as well as how consistent these frequencies can be expected to be between patients. If there is a high degree of variability in these results, as is expected, this suggests that source separation approaches should be pursued over feature detection approaches, since these spectral features associated with CAD may be quite different between individuals. In contrast, the location of the left coronary artery is relatively constant.

Another important avenue for future work involves relaxing several important limiting assumptions which are present in the numerical simulations performed as a part of this work. As discussed in Section 2.3, the simulations assumed both that damping was negligible (due to restrictions on the ANSYS elements used in the study) and the geometry was 2-D. Clearly, in the actual chest neither assumption is true. Away from resonance, the assumption of negligible damping is justifiable, since the entire domain lies in the near field of the source; waves have not propagated a far enough distance through the media for damping to be significant. Moreover, the conclusions drawn in this study were based upon the results at frequencies away from resonance, where the assumption is justifiable. In contrast, the assumption of a 2-D geometry is clearly not valid in the human body. As a result, the work described here should be seen as a preliminary first step. Performing similar simulations to calculate transfer functions for a 3-D physiologically accurate geometry is an extremely important next step, and is probably a more critical future work than the previously described artery experiments.

The expectation for the proposed 3-D simulations is that they will actually show the proposed technique to be even more feasible than the 2-D study presented here. The technique is built upon the assumption that the transfer functions between different locations on the skin surface and a given source location are significantly different. If the transfer function which populate the linear system shown in Eq. 2-2 are very similar, high condition numbers and corresponding poor error tolerance will be encountered. As a result, the proposed technique thrives and depends upon the geometric complexity of the chest. The 3-D geometry of the chest is even more complicated than the 2-D geometry. Thus, it is expected that the results from an in-depth 3-D study will reveal improved error tolerances, since there will be increased variation in the individual equations population equation Eq. 2-2 as compared to the 2-D case.

One final issue remains that has not been addressed hereto, which is the real world implementation of the proposed approach. Since the proposed approach is intended to fill the lack of a screening technique which currently leads to CAD causing 20% of all deaths in the country, it is apparent that to be practical and clinically useful, the technique must work without requiring patient specific finite element models. There are two proposed approaches to avoid requiring such a model. Recall that Eq. 2-9 relates the error in the source strengths to both the error in the forcing vector of surface velocities and the matrix of transfer functions. If the system has is relatively tolerant to surface velocity errors, it will also be resistant to errors in the matrix of transfer functions. It may be possible to build a set of generic transfer functions for different body types, and use these transfer functions in Eq. 2-3 to determine source strengths, rather than patient specific ones. The alternative to this approach would be to attempt to build the transfer functions experimentally prior to recording data by equipping the recording apparatus to be able to “ping”

the chest acoustically in the frequency range of interest at a series of locations on the chest, and calculate the transfer functions based upon the attenuated ping heard at the recording locations. Such an approach would be much more complex than the former approach, which is considered the more desirable one.

Under ideal circumstances, the recording apparatus used to implement the proposed technique would be able to take spatially continuous measurements of surface velocity over the entire chest surface, since one wants as much information as possible. In practice, this could take the form of a very light compliant band which is placed around the chest with a large number of embedded microphones/accelerometers. Unfortunately, such a device would to some extent alter the transfer functions of the chest by changing the boundary condition on the chest surface. A more desirable approach may be to use some form of laser vibrometry to record the vibration of the chest. The use of scanning laser vibrometry would have the additional advantage of being able to record the surface velocity at a large number of locations. However, regardless of the instrumentation technique used, the sites where data is recorded in any real world system will be finite, and as a result these sites will need to be chosen so as to maximize the error tolerances of the system. For example placing all the sensors very close together would lead to very poor error tolerances all of the transfer functions populating Eq. 2-2 would be very similar, leading to a poorly conditioned system with poor error tolerance. A final immediate follow-up project would be to examine the optimal choice of recording locations, so as to maximize the error tolerances of the proposed technique. Further down the road, the hope would be for the future works described here to lead to experiments in cadavers, animals, and ultimately, human patients.

4. CONCLUDING REMARKS

Coronary artery disease continues to be the leading cause of death in this country, due primarily to our inability to screen effectively for the disease. Accurate diagnostic tests exist, but their invasive nature prevents their use for general screening. Phonoangiography has the potential to be an outstanding screening test for CAD, but has historically been plague due to signal to noise problems and uncertainties regarding the actual acoustic spectra which a diseased artery can be expected to emit. This study has proposed an alternative approach to the acoustic detection of CAD which detects the sounds based upon the location of the source from which they are released, rather than the spectral content of the signals. The problems associated with uncertainty in the acoustic spectra associated with disease are rendered moot, and one need only examine the sounds produced by the coronary arteries – a noisy artery is almost certainly not a healthy artery. More to the point, the technique is intended only as a screening technique which need not make a conclusive diagnosis. To be useful it need only provoke enough suspicion to justify the risk associated with conventional, invasive tests.

A series of numerical experiments using a physiologically accurate, 2-D model of the chest were performed to test the validity of the technique. The primary concern with the proposed technique is that it would have such poor error tolerance that the technique is impractical. The results showed that while this is true for low frequencies, in the higher frequency range where many studies have reported sounds associated with CAD, the numerical errors associated with the technique are actually quite manageable. However, the strength of the conclusions that can be drawn from this initial study is limited by the assumptions made in the development of the finite element model, most notably the assumption of a 2-D model geometry. To completely verify the validity of the proposed approach, it will be necessary to perform 3-D simulations, followed by experimental validation of the approach. Based upon the behavior of the model, however, it seems likely that the technique will actually perform better in a 3-D physiologically accurate model than in the 2-D geometry. If so, then while a long road lies ahead, the concept of using source separation to screen and preliminarily diagnose CAD holds tremendous promise to revolutionize the treatment of coronary artery disease.

REFERENCES

1. Lloyd-Jones, D., et al., *Heart Disease and Stroke Statistics--2009 Update: A Report From the American Heart Association Statistics Committee and Stroke Statistics Subcommittee.* Circulation, 2009. **119**(3): p. e21-181.

2. *Heart Disease and Stroke Statistics - 2009 Update.* . 2009, American Heart Association: Dallas, Texas.

3. Guyton, A. and J. Hall, *Textbook of Medical Physiology*. 11 ed. 2006, Philadelphia: Elsevier Saunders.

4. Krupp, M.A., *Current Medical Diagnosis and Treatment*. 1982, Los Altos, CA: Lange Med. Publ.

5. Johnson, M.R., *Special diagnostic tests and procedures.* Phys. Ther., 1985. **65**(12): p. 1856-1865.

6. Redwood, D.R. and S.E. Epstein, *Uses and Limitations of Stress Testing in the Evaluation of Ischemic Heart Disease.* Circulation, 1972. **46**(6): p. 1115-1131.

7. Semmlow, J. and K. Rahalkar, *Acoustic Detection of Coronary Artery Disease.* Annual Review of Biomedical Engineering, 2007. **9**(1): p. 449-469.

8. Cheng, T.O., *Late Systolic Murmur in Coronary Artery Disease.* Chest, 1972. **61**(4): p. 346-356.

9. Cheng, T., *Diastolic murmur caused by coronary artery stenosis.* Annals of Internal Medicine, 1973. **72**: p. 543-546.

10. Sangster, F. and C. Oakley, *Diastolic murmur of coronary artery disease.* British Heart Journal, 1973. **35**(840-844).

11. Mazumdar, J.N., *Biofluid Mechanics*. 2004, London: World Scientific.

12. Ku, D.N., *Blood Flow in Arteries.* Annual Review of Fluid Mechanics, 2003. **29**(1): p. 399-434.

13. Cengel, Y. and J. Cimbala, *Fluid Mechanics: Fundamentals and Applications*. 1 ed. 2006, New York: McGraw Hill Higher Education.

14. Clark, C., *The propagation of turbulence produced by a stenosis.* Journal of Biomechanics, 1980. **13**(7): p. 591-604.

15. Clark, C., *The fluid mechanics of aortic stenosis--I. Theory and steady flow experiments.* Journal of Biomechanics, 1976. **9**(8): p. 521-528.

16. Clark, C., *Turbulent wall pressure measurements in a model of aortic stenosis.* Journal of Biomechanics, 1977. **10**(8): p. 461-472.

17. Yongchareon, W. and D.F. Young, *Initiation of turbulence in models of arterial stenoses.* Journal of Biomechanics, 1979. **12**(3): p. 185-189, 191-196.

18. Young, D.F. and F.Y. Tsai, *Flow characteristics in models of arterial stenoses -- I. Steady flow.* Journal of Biomechanics, 1973. **6**(4): p. 395-402, IN3, 403-410.

19. Young, D.F. and F.Y. Tsai, *Flow characteristics in models of arterial stenoses -- II. Unsteady flow.* Journal of Biomechanics, 1973. **6**(5): p. 547-559.

20. Ahmed, S.A. and D.P. Giddens, *Velocity measurements in steady flow through axisymmetric stenoses at moderate Reynolds numbers.* Journal of Biomechanics, 1983. **16**(7): p. 505-507, 509-516.

21. Ahmed, S.A. and D.P. Giddens, *Pulsatile poststenotic flow studies with laser Doppler anemometry.* Journal of Biomechanics, 1984. **17**(9): p. 695-705.

22. Khalifa, A.M.A. and D.P. Giddens, *Characterization and evolution of poststenotic flow disturbances.* Journal of Biomechanics, 1981. **14**(5): p. 279-296.

23. Lieber, B.B. and D.P. Giddens, *Post-stenotic core flow behavior in pulsatile flow and its effects on wall shear stress.* Journal of Biomechanics, 1990. **23**(6): p. 597-605.

24. Cassanova, R.A. and D.P. Giddens, *Disorder distal to modeled stenoses in steady and pulsatile flow.* Journal of Biomechanics, 1978. **11**(10-12): p. 441-453.

25. Ku, D.N., *Blood Flow in Arteries.* Annual Review of Fluid Mechanics, 1997. **29**(1): p. 399-434.

26. Fredberg, J.J., *Origin and character of vascular murmurs: Model studies.* The Journal of the Acoustical Society of America, 1977. **61**(4): p. 1077-1085.

27. Tobin, R.J. and I.-D. Chang, *Wall pressure spectra scaling downstream of stenoses in steady tube flow.* Journal of Biomechanics, 1976. **9**(10).

28. Stroud, J.S., S.A. Berger, and D. Saloner, *Numerical Analysis of Flow Through a Severely Stenotic Carotid Artery Bifurcation.* Journal of Biomechanical Engineering, 2002. **124**(1): p. 9-20.

29. Varghese, S.S., S.H. Frankel, and P.F. Fischer, *Modeling Transition to Turbulence in Eccentric Stenotic Flows.* Journal of Biomechanical Engineering, 2008. **130**(1): p. 014503-7.

30. Mittal, R., S.P. Simmons, and F. Najjar, *Numerical study of pulsatile flow in a constricted channel.* Journal of Fluid Mechanics, 2003. **485**(-1): p. 337-378.

31. Sherwin, S.J. and H.M. Blackburn, *Three-dimensional instabilities and transition of steady and pulsatile axisymmetric stenotic flows.* Journal of Fluid Mechanics, 2005. **533**(-1): p. 297-327.

32. Varghese, S.S., S.H. Frankel, and P.F. Fischer, *Direct numerical simulation of stenotic flows. Part 1. Steady flow.* Journal of Fluid Mechanics, 2007. **582**(-1): p. 253-280.

33. Varghese, S.S., S.H. Frankel, and P.F. Fischer, *Direct numerical simulation of stenotic flows. Part 2. Pulsatile flow.* Journal of Fluid Mechanics, 2007. **582**(-1): p. 281-318.

34. Varghese, S.S. and S.H. Frankel, *Numerical Modeling of Pulsatile Turbulent Flow in Stenotic Vessels.* Journal of Biomechanical Engineering, 2003. **125**(4): p. 445-460.

35. Karri, S. and P.P. Vlachos, *Time-Resolved DPIV Investigation of Pulsatile Flow in Symmetric Stenotic Arteries - Effects of Phase Angle.* Journal of Biomechanical Engineering, 2010. **132**(3).

36. Akay, Y., et al., *Dynamics of the sounds caused by partially occluded femoral arteries in dogs.* Annals of Biomedical Engineering, 1994. **22**(5): p. 493-500.

37. Semmlow, J.L., et al., *Coronary artery disease - correlates between diastolic auditory characteristics and coronary artery stenosis.* IEEE Trans. Biomed. Eng., 1998. **30**: p. 136-139.

38. Borisyuk, A.O., *Experimental Study of Noise Produced by Steady Flow through a Simulated Vascular Stenosis.* Journal of Sound and Vibration, 2002. **256**(3): p. 475-498.

39. Akay, M., et al., *Detection of coronary occlusions using autoregressive modeling of diastolic heart sounds.* Biomedical Engineering, IEEE Transactions on, 1990. **37**(4): p. 366-373.

40. Akay, M., et al., *Analysis of diastolic heart sounds before and after angioplasty*, in *IEEE EMBS 10th Ann. Int. Conf.* 1988: New Orleans.

41. Mohler, S., *Sonospectrographic analyzer*. 2000: United States.

42. Yazicioglu, Y., et al., *Acoustic radiation from a fluid-filled, subsurface vascular tube with internal turbulent flow due to a constriction.* The Journal of the Acoustical Society of America, 2005. **118**(2): p. 1193-1209.

43. Wang, J.Z., et al., *Modeling sound generation in stenosed coronary arteries.* Biomedical Engineering, IEEE Transactions on, 1990. **37**(11): p. 1087-1094.

44. Goral-Wojcicka, A., et al., *On the acoustic phenomena produced by turbulence in the flowing blood* Polish J. Med. Phys. Eng., 2002. **8**: p. 29-35.

45. Semmlow, J.L., M. Akay, and W. Welkowitz, *Noninvasive detection of coronary artery disease using parametric spectral analysis methods.* IEEE Engr. Med. Biol. Mag., 1990. **9**: p. 33-36.

46. Akay, M., et al., *Application of the ARMA method to acoustic detection of coronary artery disease*. Med. Biol. Eng. Comput., 1991. **29**: p. 365-372.

47. Güler, I., M. Kiymik, and N. Güler, *Order determination in autoregressive modeling of diastolic heart sounds.* Journal of Medical Systems, 1996. **20**(1): p. 11-17.

48. Akay, M., et al., *Noninvasive acoustical detection of coronary artery disease using the adaptive line enhancer method.* Medical and Biological Engineering and Computing, 1992. **30**(2): p. 147-154.

49. Akay, M., et al., *Application of adaptive filters to noninvasive acoustical detection of coronary occlusions before and after angioplasty.* Biomedical Engineering, IEEE Transactions on, 1992. **39**(2): p. 176-184.

50. Akay, Y.M., et al., *Noninvasive acoustical detection of coronary artery disease: a comparative study of signal processing methods.* Biomedical Engineering, IEEE Transactions on, 1993. **40**(6): p. 571-578.

51. Akay, M., et al., *Application of adaptive FTF/FAEST zero tracking filters to noninvasive characterization of the sound pattern caused by coronary artery stenosis before and after angioplasty.* Annals of Biomedical Engineering, 1993. **21**(1): p. 9-17.

52. Akay, M., et al., *Noninvasive characterization of the sound pattern caused by coronary artery stenosis using FTF/FAEST zero tracking filters: Normal/abnormal study.* Annals of Biomedical Engineering, 1993. **21**(2): p. 175-182.

53. Shertukde, H. and R. Shertukde, *Apparatus and method for noninvasive diagnosing of coronary artery disease*. 2005: United States.

54. Padmanhban, V. and J. Semmlow, *Dynamical analysis of diastolic heart sounds associated with coronary artery disease.* Annals of Biomedical Engineering, 1994. **22**: p. 264-271.

55. Xiao, Y., et al., *The phonocardiogram exercise test.* Engineering in Medicine and Biology Magazine, IEEE, 1999. **18**(4): p. 111-115.

56. Zhao, Z. *Noninvasive Diagnosis of Coronary Artery Disease Based on Instantaneous Frequency of Diastolic Murmurs and SVM*. in *Engineering in Medicine and Biology Society, 2005. IEEE-EMBS 2005. 27th Annual International Conference of the*. 2005.

57. Yoshida, H., H. Shino, and K. Yana. *Instantaneous frequency analysis of systolic murmur for phonocardiogram*. in *Engineering in Medicine and Biology Society, 1997. Proceedings of the 19th Annual International Conference of the IEEE*. 1997.

58. Owsley, N.L. *Array phonocardiography*. in *Adaptive Systems for Signal Processing, Communications, and Control Symposium 2000. AS-SPCC. The IEEE 2000*. 2000.

59. Owsley, N.L. and A.J. Hull, *Beamformed Nearfield Imaging of a Simulated Coronary Artery Containing a Stenosis* IEEE Trans. Biomed. Eng., 1998. **17**(6).

60. Kinsler, L.E. and A.R. Frey, *Fundamentals of Acoustics*. 2 ed. 1962, New York: John Wiley & Sons.

61. Mansy, H.A., et al., *Pneumothorax detection using pulmonary acoustic transmission measurements.* Med Biol Eng Comput, 2002. **40**(5): p. 520-5.

62. Royston, T.J., et al., *Modeling sound transmission through the pulmonary system and chest with application to diagnosis of a collapsed lung.* Journal of the Acoustical Society of America, 2002. **111**(4): p. 1931-1946.

63. Roache, P.J., *Verification and Validation in Computational Science and Engineering*. 1998, Albuquerque, New Mexico: Hermosa Publishers.

64. Friedberg, S.H., A. Insel, J., and L. Spence, E., *Linear Algebra*. 4 ed. 2003, Upper Saddle River, New Jersey: Prentice-Hall, Inc.

APPENDICES

A. DESCRIPTION & ANSYS IMPLEMENTATION OF ACOUSTIC POINT SOURCES

The ANSYS Fluid 29/30 elements use pressure as their degree of freedom. In standard FEA, forces can be applied to nodes; with these acoustic elements FLOW loads are applied. This flow load represents the pumping of fluid in and out of the system at the node, and has units of mass/time^2. For a 2-D geometry, the strength of the FLOW load can be calculated by:

$$FLOW = \pi R^2 \rho \frac{d^2 u}{dt^2} \qquad \text{Eq. A-1}$$

here R represents the radius of a circular point source so that πR^2 represents the area of the point source. u represents the radial displacement of the perimeter of the point source. In other words, u represents how far in or out the edge of the circular point source has moved. Thus, the second time derivative of u represents the acoustic particle acceleration. In the case of this work the primary interest is the acoustic particle velocity. If we assume that the radial displacement u is harmonic, then FLOW load can be calculated by:

$$FLOW = j\omega \pi R^2 \rho \frac{du}{dt} \qquad \text{Eq. A-2}$$

This is the expression used in this work when calculating the acoustic transfer functions.

B. ADDITIONAL RESULTS

In Section 3.1, the acoustic transfer functions associated with point sources located in the left coronary artery, the right coronary artery, and the left dorsal lung are shown. This portion of the appendix contains the transfer functions associated with the point sources at the remainder of the locations listed in Table 2-2. Figure B-1 through Figure B-4 present the transfer functions for the remainder of the sources associated with the cardiovascular system, while Figure B-5 through Figure B-11 represent the results for the remainder of the sources associated with the respiratory system.

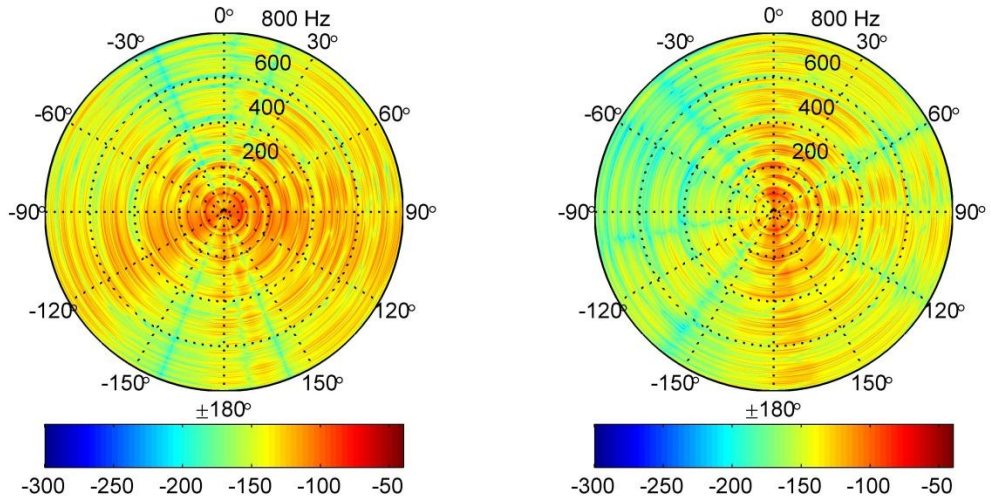

Figure B-1: *left:* x-velocity component acoustic transfer function corresponding to a point source located in the left atrium. *right:* acoustic transfer function for the y-component of velocity. Radial coordinate corresponds to frequency, while the angle coordinate corresponds to surface position, measured by angle from the anterior mid-sagittal plane. Colorbar units: dB.

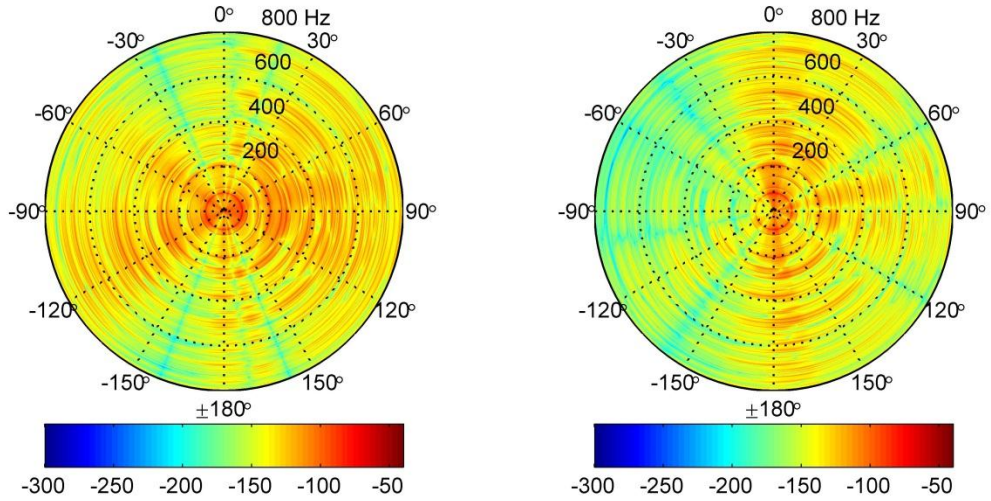

Figure B-2: *left:* x-velocity component acoustic transfer function corresponding to a point source located in the right atrium. *right:* acoustic transfer function for the y-component of velocity. Radial coordinate corresponds to frequency, while the angle coordinate corresponds to surface position, measured by angle from the anterior mid-sagittal plane. Colorbar units: dB.

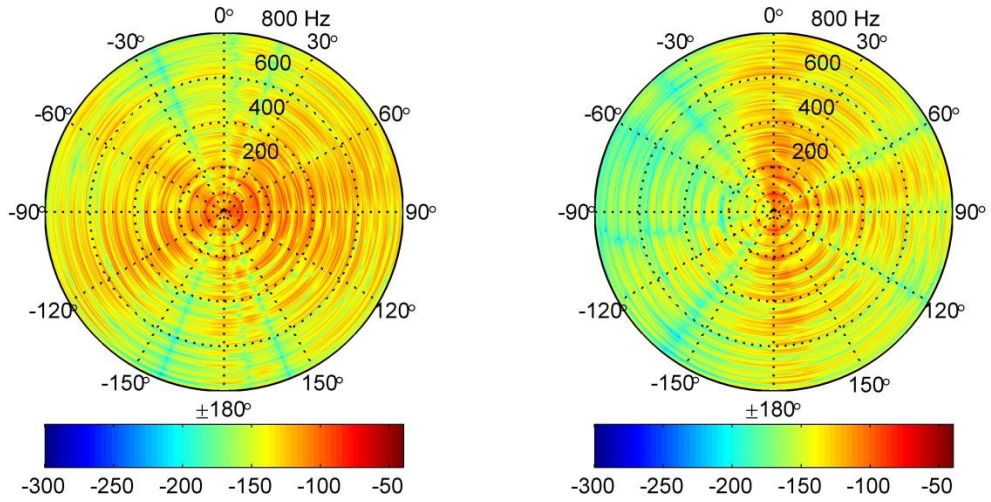

Figure B-3: *left:* x-velocity component acoustic transfer function corresponding to a point source located in the right ventricle. *right:* acoustic transfer function for the y-component of velocity. Radial coordinate corresponds to frequency, while the angle coordinate corresponds to surface position, measured by angle from the anterior mid-sagittal plane. Colorbar units: dB.

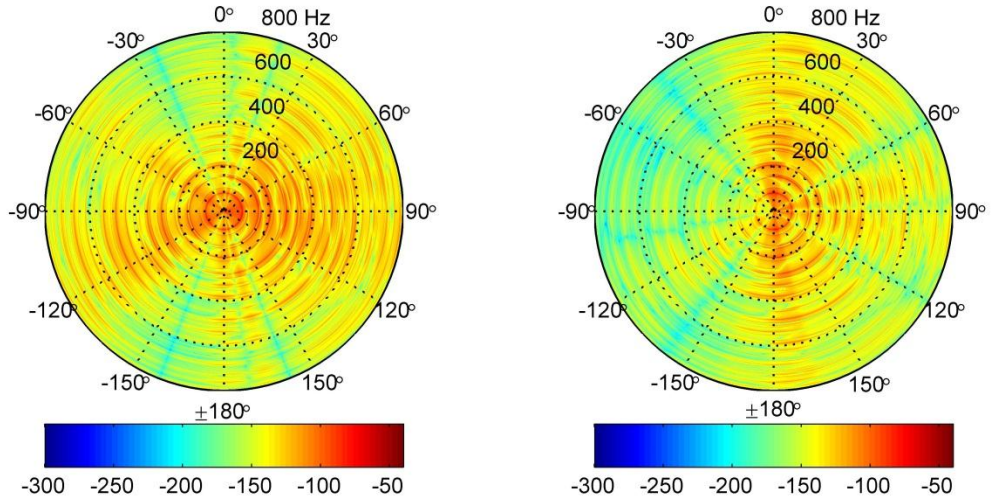

Figure B-4: *left:* x-velocity component acoustic transfer function corresponding to a point source located in the aorta. *right:* acoustic transfer function for the y-component of velocity. Radial coordinate corresponds to frequency, while the angle coordinate corresponds to surface position, measured by angle from the anterior mid-sagittal plane. Colorbar units: dB.

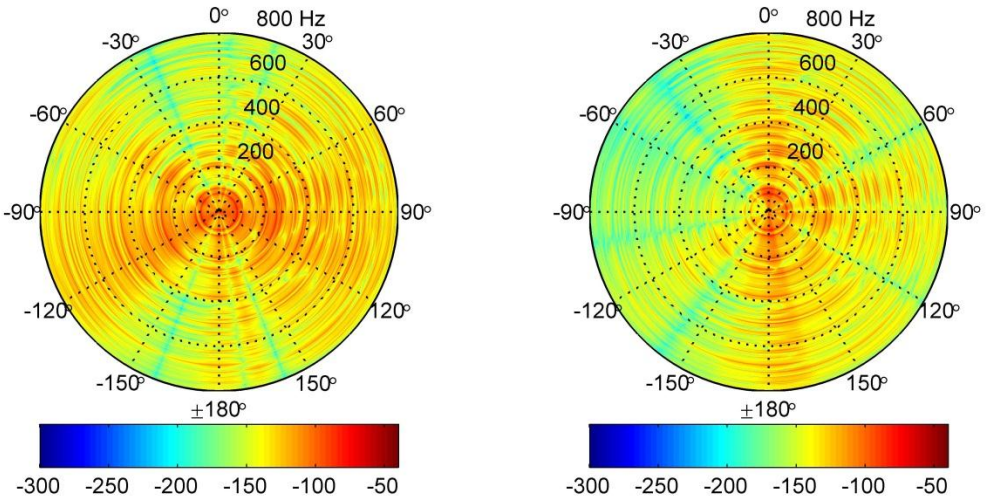

Figure B-5: *left:* x-velocity component acoustic transfer function corresponding to a point source located in the left primary bronchus. *right:* acoustic transfer function for the y-component of velocity. Radial coordinate corresponds to frequency, while the angle coordinate corresponds to surface position, measured by angle from the anterior mid-sagittal plane. Colorbar units: dB.

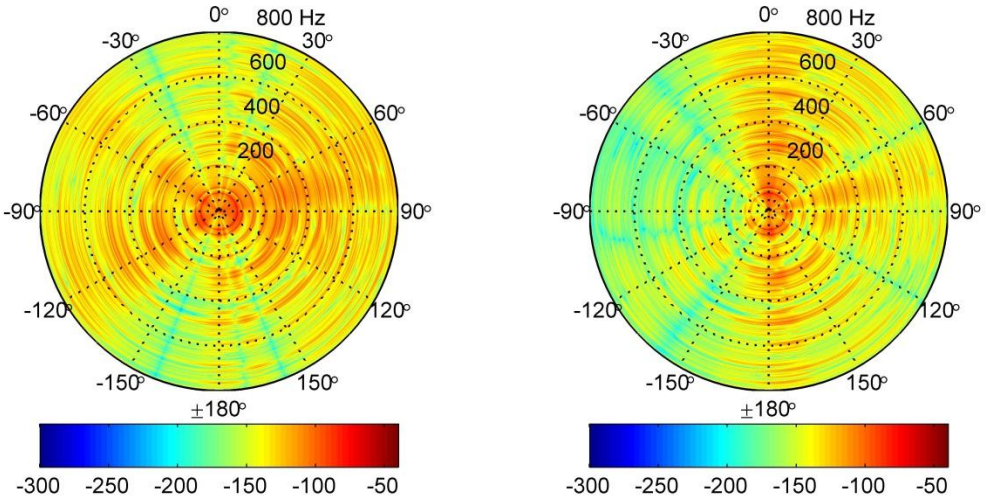

Figure B-6: *left:* x-velocity component acoustic transfer function corresponding to a point source located in the right primary bronchus. *right:* acoustic transfer function for the y-component of velocity. Radial coordinate corresponds to frequency, while the angle coordinate corresponds to surface position, measured by angle from the anterior mid-sagittal plane. Colorbar units: dB.

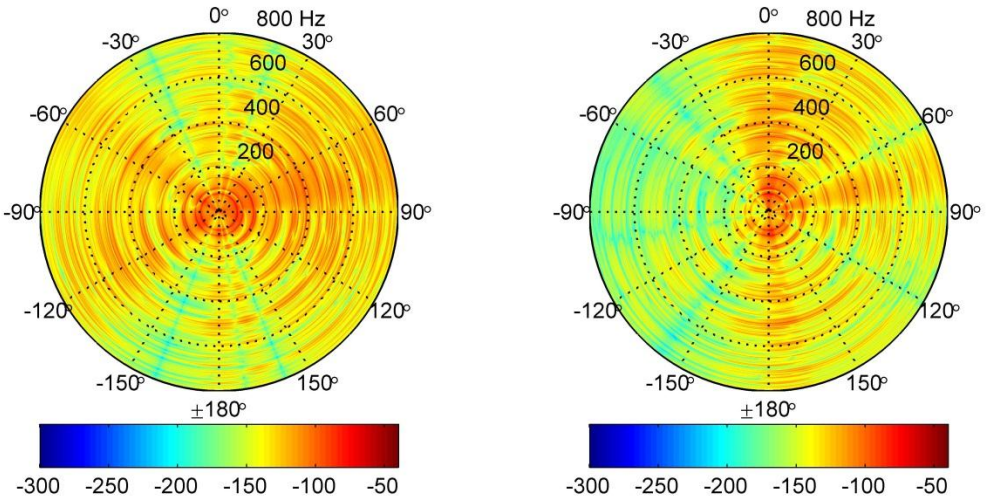

Figure B-7: *left:* x-velocity component acoustic transfer function corresponding to a point source located in the right dorsal lung. *right:* acoustic transfer function for the y-component of velocity. Radial coordinate corresponds to frequency, while the angle coordinate corresponds to surface position, measured by angle from the anterior mid-sagittal plane. Colorbar units: dB.

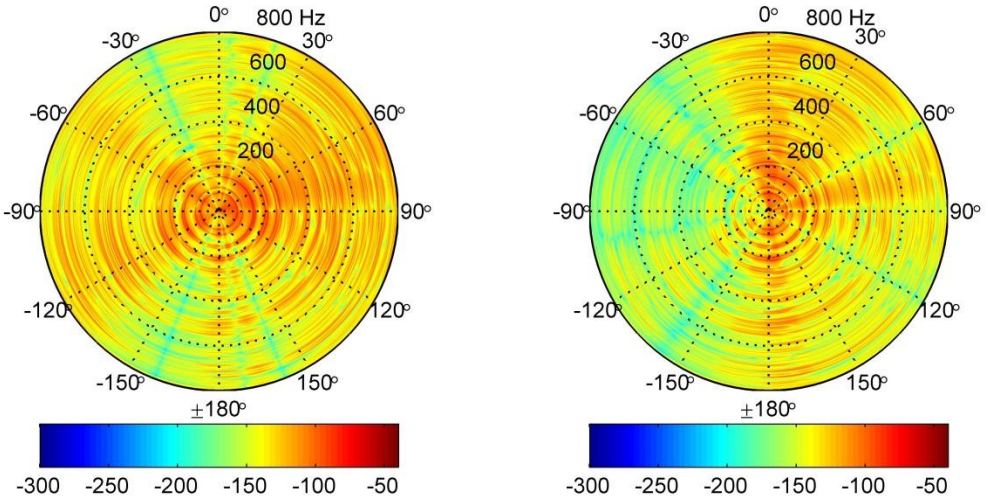

Figure B-8: *left:* x-velocity component acoustic transfer function corresponding to a point source located in the left mid lung. *right:* acoustic transfer function for the y-component of velocity. Radial coordinate corresponds to frequency, while the angle coordinate corresponds to surface position, measured by angle from the anterior mid-sagittal plane. Colorbar units: dB.

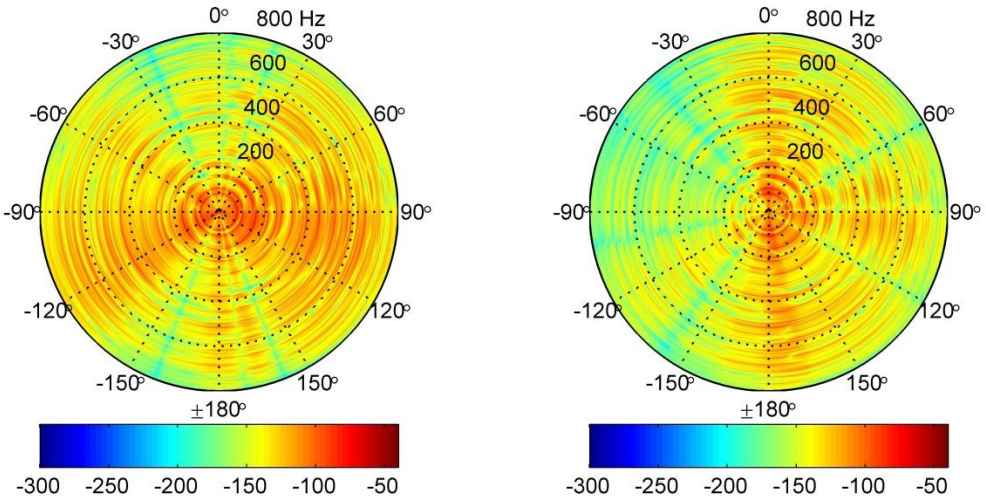

Figure B-9: *left:* x-velocity component acoustic transfer function corresponding to a point source located in the right mid lung. *right:* acoustic transfer function for the y-component of velocity. Radial coordinate corresponds to frequency, while the angle coordinate corresponds to surface position, measured by angle from the anterior mid-sagittal plane. Colorbar units: dB.

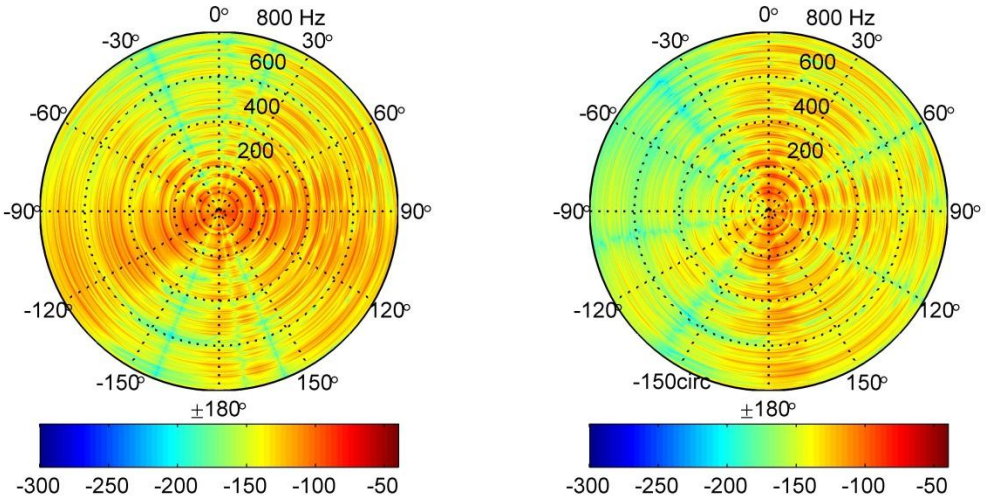

Figure B-10: *left:* x-velocity component acoustic transfer function corresponding to a point source located in the left ventral lung. *right:* acoustic transfer function for the y-component of velocity. Radial coordinate corresponds to frequency, while the angle coordinate corresponds to surface position, measured by angle from the anterior mid-sagittal plane. Colorbar units: dB.

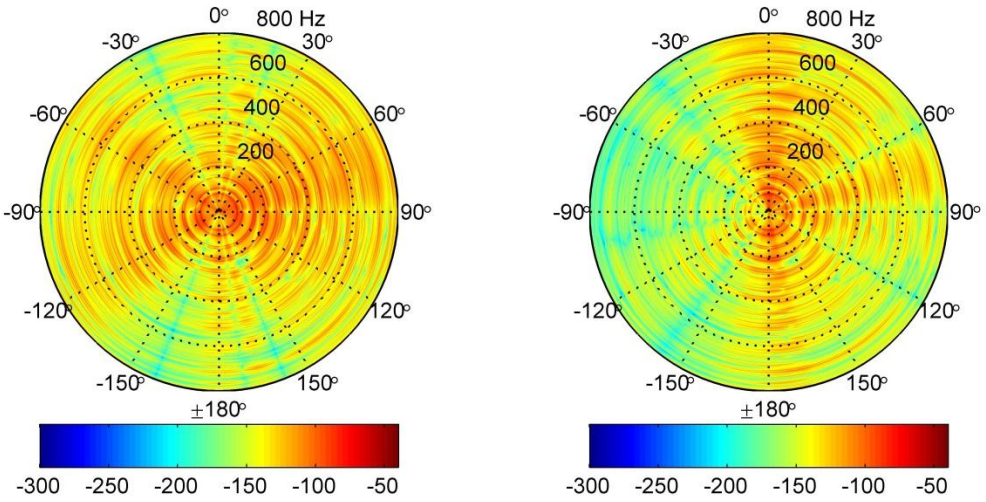

Figure B-11: *left:* x-velocity component acoustic transfer function corresponding to a point source located in the left atrium. *right:* acoustic transfer function for the y-component of velocity. Radial coordinate corresponds to frequency, while the angle coordinate corresponds to surface position, measured by angle from the anterior mid-sagittal plane. Colorbar units: dB.